

AD-A284 335

MENTATION PAGE

Form Approved
OMB No. 0704-0168

Estimated to average 1 hour per response, including the time for reviewing instructions, searching existing data sources, gathering and reviewing the collection of information, Send comments regarding this burden estimate or any other aspect of this burden, to Washington Headquarters Services, Directorate for Information Operations and Reports, 1215 Jefferson Davis Highway, Suite 1204, Arlington, VA 22202-4302, and to the Office of Management and Budget, Paperwork Reduction Project (0704-0168), Washington, DC 20503.

1. AGENCY USE ONLY (Leave blank)		2. REPORT DATE Sep 94		3. REPORT TYPE AND DATES COVERED	
4. TITLE AND SUBTITLE Effects of Sulfate Aerosol on the Central Pennsylvania Surface Shortwave Radiation Budget				5. FUNDING NUMBERS	
6. AUTHOR(S) Phillip W. Guimond				7. PERFORMING ORGANIZATION NAME(S) AND ADDRESS(ES) AFIT Students Attending: Pennsylvania State University	
9. SPONSORING/MONITORING AGENCY NAME(S) AND ADDRESS(ES) DEPARTMENT OF THE AIR FORCE AFIT/CI 2950 P STREET WRIGHT-PATTERSON AFB OH 45433-7765				8. PERFORMING ORGANIZATION REPORT NUMBER AFIT/CI/CIA 94-123	
10. SPONSORING/MONITORING AGENCY REPORT NUMBER					
11. SUPPLEMENTARY NOTES					
12a. DISTRIBUTION/AVAILABILITY STATEMENT Approved for Public Release IAW 190-1 Distribution Unlimited MICHAEL M. BRICKER, SMSgt, USAF Chief Administration				12b. DISTRIBUTION CODE	
13. ABSTRACT (Maximum 200 words)				<div data-bbox="1096 1211 1470 1486" data-label="Image"> </div>	
14. SUBJECT TERMS				15. NUMBER OF PAGES 99	
16. PRICE CODE				17. SECURITY CLASSIFICATION OF REPORT	
18. SECURITY CLASSIFICATION OF THIS PAGE		19. SECURITY CLASSIFICATION OF ABSTRACT		20. LIMITATION OF ABSTRACT	

DTIC QUALITY INSPECTED 3

94 9 14 078

94-29926

113

The Pennsylvania State University

The Graduate School

Department of Meteorology

EFFECTS OF SULFATE AEROSOL ON
THE CENTRAL PENNSYLVANIA SURFACE
SHORTWAVE RADIATION BUDGET

A Thesis in

Meteorology

by

Philip W. Guimond

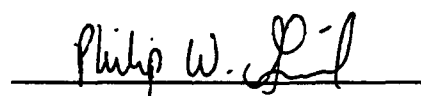
Accession For		↓
NTIS - CRA21		↓
DUE - TAG		↓
S. H. H. H. H.		↓
Justification		
By		
Distribution /		
Availability Codes		
Dist	Avail. and/or Special	
A-1		

Submitted in Partial Fulfillment
of the Requirements
for the Degree of

Master of Science

December 1994

I grant The Pennsylvania State University the nonexclusive right to use this work for the University's own purposes and to make single copies of the work available to the public on a not-for-profit basis if copies are not otherwise available.

A handwritten signature in dark ink, reading "Philip W. Guimond", is written over a horizontal line. The signature is cursive and stylized, with the first name "Philip" and last name "Guimond" clearly legible, and "W." in the middle.

Philip W. Guimond

We approve the thesis of Philip W. Guimond.



Thomas P. Ackerman
Associate Professor of Meteorology
Thesis Advisor

Date of Signature

12 Aug 94



Bruce A. Albrecht
Professor of Meteorology

12 Aug 94



Dennis W. Thomson
Professor of Meteorology
Head of the Department of Meteorology

12.8.94

TABLE OF CONTENTS

LIST OF FIGURES.	v
LIST OF TABLES.	viii
ACKNOWLEDGMENTS.	ix
 Chapter 1. INTRODUCTION.	 1
1.1. Sulfate Aerosols.	2
1.2. Experimental Conditions.	4
 Chapter 2. COMPARISON OF ROTATING SHADOWBAND RADIOMETER AND SUN PHOTOMETER OPTICAL DEPTH MEASUREMENTS.	 9
 Chapter 3. CALCULATION OF SURFACE INSOLATION.	 29
3.1. Boundary layer extent.	31
3.2. Scattering coefficient.	32
3.3. Relative humidity profile.	33
3.4. Vertical aerosol distribution.	34
3.5. Model description and verification.	48
 Chapter 4. COMPARISON OF INSOLATION WITH AND WITHOUT AEROSOL PRESENT.	 62
 Chapter 5. CONCLUSIONS AND RECOMMENDATIONS.	 91

LIST OF FIGURES

Figure	Page
2.1 Scatter plot of optical depth data obtained by RSR at 415 nm versus that acquired by sun photometer at 400 nm. Each point denotes a ten-minute optical depth average.	15
2.2 Same as in Figure 2.1, but with wavelengths of 500 nm versus 519 nm.	16
2.3 Same as in Figure 2.1, but with wavelengths of 610 nm versus 609 nm.	17
2.4 Same as in Figure 2.1, but with wavelengths of 665 nm versus 670 nm.	18
2.5 Same as in Figure 2.1, but with wavelengths of 862 nm versus 872 nm.	19
2.6 Scatter plot of RSR optical depth data gathered at 415 nm versus that acquired by sun photometer at 400 nm. Each point represents data averaged for an entire day; periods of good data range from one to three hours. Vertical and horizontal error bars represent standard deviations of RSR and sun photometer data, respectively. Best-fit equation (linear regression with y-intercept forced to zero) and correlation coefficient are shown at upper left.	21
2.7 Same as in Figure 2.6, but with wavelengths of 500 nm versus 519 nm.	22
2.8 Same as in Figure 2.6, but with wavelengths of 610 nm versus 609 nm.	23
2.9 Same as in Figure 2.6, but with wavelengths of 665 nm versus 670 nm.	24
2.10 Same as in Figure 2.6, but with wavelengths of 862 nm versus 872 nm.	25

LIST OF FIGURES (continued)

Figure	Page
2.11. Optical depth offset between sun photometer and RSR. The data curve is shown together with a best-fit curve, which shows a relationship between $\Delta\tau$ and λ similar to that between scattering and wavelength.	26
3.1. Scatter plot of water vapor content as measured by radiosonde versus that evaluated (averaged over the period in question) by the microwave radiometer. Best-fit equation and correlation coefficient are at upper left.	35
3.2. Comparison of shapes of $\tau(\lambda)$ and $\sigma_{\text{scat}}(\lambda)$ plotted versus wavelength. Data are from 15 Aug 1993.	44
3.3. Same as Figure 3.2 except from 22 Aug 1993.	45
3.4. Same as Figure 3.2 except from 23 Aug 1993.	46
3.5. Same as Figure 3.2 except from 26 Aug 1993.	47
3.6. A comparison of the sun photometer data points and the curve following the equation $\tau = 0.219(\lambda^{-1.71})$. Data shown are from 15 August 1993 at 0827 EST.	52
3.7. A scatter plot of calculated vs. measured fluxes. The line $y = 1.025x$ is the expected result given the use of a slightly larger spectrum by the model than by the pyranometer.	56
3.8. Same as in Figure 3.7, but with marginal data from August 15 and 26 deleted.	58
3.9. Surface flux vs. time plot from August 26.	59
3.10. A histogram of fractional error distribution indicates that nearly all points have errors of less than three percent.	61

LIST OF FIGURES (continued)

Figure	Page
4.1. The optical depth at 519 nm is shown for all days of the experiment.	65
4.2. Relative humidity is plotted as a function of time.	66
4.3. Surface flux computed with and without aerosol present is shown for August 15.	68
4.4. Same as Figure 4.3, but for August 22.	69
4.5. Same as Figure 4.3, but for August 23.	70
4.6. Same as Figure 4.3, but for August 26.	71
4.7. Net flux change due to aerosol as a function of time.	73
4.8. Fractional flux change due to aerosol as a function of time.	76
4.9. Net flux loss is plotted against optical depth.	77
4.10. Fractional flux loss is shown as a function of optical depth.	79
4.11. Data points from Figure 4.10 are shown with a best-fit curve.	80
4.12. Same as Figure 4.11, but with y-intercept forced to zero.	82
4.13. Optical depth is shown plotted against relative humidity.	84
4.14. Net flux loss is shown as a function of relative humidity.	87
4.15. Fractional flux loss is shown as a function of relative humidity.	89

LIST OF TABLES

Table	Page
1.1. Instrumentation deployed and variables measured during the Rock Springs experiment.	7
2.1. Wavelengths and corresponding zero-airmass calibration voltages of sun photometer.	11
3.1. Using various values of β , the effect of assuming the maximum radius to be 1, 10, or 100 μm is shown to be negligible on the mean radius (Davies, 1974).	40
3.2. Calculated values of r_M , σ_g , and v^* using Mie theory.	42

ACKNOWLEDGMENTS

Many people have contributed to the completion of this thesis; these include my family, the Penn State Meteorology Department, and AFIT personnel and students. I would like to extend special thanks to several of these people.

My wife Sarah has given me encouragement and love for our time here, even during those frequent times when I was impossible to get along with. My love and appreciation for her is enormous, and I couldn't have accomplished this paper without her.

My parents have been in my corner for thirty years and counting now. They have faith in my abilities even when I don't, and I am fortunate to have them always behind me.

Several students and staff have gone out of their way to assist me. Among these are Adrian George, Chuck Pavloski, Seiji Kato, Jorge Valero, Richard Penc, Laurie Bothell, and Eugene Clothiaux. Thanks to all of you for helping me contend with any difficulties. I would also like to thank Joe Michalsky at SUNY-Albany for his gracious support, as well as my advisors here.

My fellow AFIT students and I have gotten to know each other quite well during our time here. Struggling through classes was no fun, but at least I knew there were people I could count on to come to my rescue.

Finally, I am grateful to the United States Air Force for allowing me the opportunity to pursue a master's degree.

Chapter 1

INTRODUCTION

Atmospheric aerosols impact the earth's surface radiation budget. These tiny particles, whether derived from natural or anthropogenic sources, whether in the solid or liquid phase, interact with solar and terrestrial radiation. In some cases, absorption by the aerosol may occur, warming the air nearby. In other instances, the radiation may be scattered; i.e., its energy is preserved but its direction is altered. The combination of these processes modifies the distribution of energy in the lower troposphere and at the surface. These interactions depend strongly on the size distribution, chemical composition, and shapes of the particles, and are currently poorly understood.

Given that aerosols influence radiative transfer, it follows logically that they affect climate as well. This theory has been tested in various models over the last two decades, chiefly with respect to stratospheric volcanic aerosol (e.g., Pollack et al., 1976; Hansen et al., 1978). Fewer studies have been conducted on the regional climate effects resulting from anthropogenic aerosol emissions (e.g., Ackerman, 1977). However, with the recent increased interest in global climate matters, many papers have addressed the theoretical links between aerosol and climate (e.g., Schneider, 1989; Corell, 1990; Penner and Mulholland, 1991; Charlson et al., 1992). Several conclusions can be drawn from this body of work. First, the effect of tropospheric aerosol on climate can be divided into

direct radiative effects and indirect effects of aerosol on cloud microphysics. Second, the direct effects are highly dependent on aerosol size distribution, which is a strong function of relative humidity. Third, inferences drawn in this paper are unlikely to apply to other regions as easily as, for instance, conclusions regarding CO₂, given the highly variable nature of aerosol concentrations. Fourth, the indirect effects are strongly tied to boundary layer convection and associated clouds such as stratocumulus, because a change in aerosol distribution is tantamount to a modification of the cloud condensation nuclei (CCN) for such clouds. Finally, current model results contain large uncertainties due to a lack of high-quality aerosol data which address the issues of aerosol concentrations, sizes, and interaction with boundary layer processes. The research presented here is aimed at reducing some of these uncertainties.

1.1. Sulfate Aerosols.

Several recent studies (Charlson et al., 1992; Kaufman and Chou, 1993) that claim direct radiative sulfate effects may oppose warming produced by increased carbon dioxide intrigue climatologists. However, as Penner (1990) and Charlson et al. (1992) have pointed out, the potential large-scale climatic impacts of aerosol are apt to differ greatly from those of CO₂. Because CO₂ is well mixed, increases in its concentration will likely produce a relatively uniform warming effect. SO₂ and its related aerosol products, on the other hand, tend to be highly

"patchy" on a global scale, implying that their effects should be studied in an area that is subject to large, anthropogenic perturbations. The northeastern United States clearly can be considered such a "patch" that comes and goes periodically (Husar et al., 1976; Ball and Robinson, 1982; Fraser et al., 1984). In this region, the ambient sulfate loading represents a good surrogate measure of anthropogenic influences since the natural sources of sulfur here are very weak. Rural central Pennsylvania is a nearly ideal site for sulfate aerosol investigation because it is centrally located within this large, perturbed region but has no large sulfur sources in its immediate vicinity.

As Charlson et al. (1992) have clearly outlined, particles produce both direct and indirect radiative influences. The direct effects derive from the interaction of solar radiation with the particles under clear skies; the particles reflect some of the sunlight back to space, reducing the surface flux (Ball and Robinson, 1982). Though some absorption can occur (Hänel et al., 1980), it appears to be important only in polar regions (Blanchet, 1989). The indirect effect (Twomey et al., 1984) arises as a result of the solubility of most particles in aqueous solutions and the competition among these particles for the available water vapor during cloud formation (Twomey, 1959). The number of aerosol particles, which serve as CCN, is proportional to the number of drops formed (assuming constant liquid water content, the larger number of CCN would result in greater competition for available water, and thus smaller but more drops); a cloud with more drops more effectively scatters radiation. In addition, the cloud lifetime

is likely enhanced with high numbers of CCN; the inverse relationship between number concentration and drop size stabilizes the cloud structure and restricts precipitation (Albrecht, 1989). Thus, clouds formed in the presence of more CCN reflect sunlight more efficiently and for longer periods.

The focus of this work will be solely on the direct effects of sulfate aerosol on the radiation budget, both spectrally and as a whole, of central Pennsylvania. The goals are to calculate the net loss of surface flux due strictly to the interaction of sulfate aerosol with shortwave radiation, and to determine whether the attenuation can be easily resolved as a function of relative humidity and/or visibility, two commonly measured meteorological variables. If a strong correlation can be discovered, the ultimate goal is that boundary-layer sulfate haze may be relatively easily parameterized in general circulation models.

1.2. Experimental Conditions.

To study sulfate haze and its possible effects on climate, it was necessary to 1) conceive an experiment; 2) determine the instruments/conditions needed to proceed successfully; and 3) make reasonable physical assumptions. Simply stated, the concept was to measure net surface flux, wavelength-dependent optical depths, scattering coefficient, boundary layer height, and total water vapor. The model being used requires as input all of these variables except surface flux to calculate surface flux itself. The model output flux can then be

compared with the measured flux, and the effects produced by the aerosol can be inferred.

The next step was to consider the instrumentation necessary. Already in place at the research site at Rock Springs were a microwave radiometer and a ceilometer, both capable of continuous operation; the former is used to measure integrated water vapor, and the latter to estimate the boundary layer height. The Rock Springs site is located approximately ten miles southwest of The Pennsylvania State University's main campus. It is surrounded on all sides by fields used for agricultural research, and bounded on the south by a mountain ridge about 2 km away rising less than 1000 m above the site itself. A rotating shadowband radiometer (RSR), functional in all weather, was also at Rock Springs and working prior to the experiment. The RSR measures total, direct, and diffuse flux, as well as spectrally-resolved components at four wavelengths (Michalsky et al., 1986).

In addition to the apparatus described above, it was decided to deploy several more instruments. First, a portable ten-channel sun photometer was necessary to complement the RSR; while the latter can be operated continuously, the former requires attention but provides spectrally-resolved direct solar radiance at ten wavelengths between 380 and 1030 nm. The ten-channel sun photometer's output allows calculation of aerosol size distribution (King et al., 1978), and its 940-nm channel can be used to continuously monitor the column water vapor concentration. Also important to this research were a nephelometer

to measure total scattering and backscatter coefficients at the surface, and radiosonde launches to yield information about the atmosphere's vertical profile.

The final decision regarding equipment involved a computer and an analog-digital converter capable of carrying sixteen signals at a time. To ensure as thorough a data set as possible, with basic meteorological as well as radiometric measurements, the computer was configured as shown in Table 1.1, with readings taken every one second and averaged every 30 seconds. The set of three Eppley pyranometers, which measure solar flux from 295-2800 nm, 395-2800 nm, and 695-2800 nm, were selected to allow an inspection of total solar radiation, all insolation except ultraviolet, and only near infrared energy, respectively. The downward longwave flux was measured with an Eppley pyrgeometer.

The next key issue was deciding what meteorological conditions were needed to optimize the study of direct sulfate effects. Several criteria were judged to be crucial. First, skies had to be cloud-free, to avoid confusing direct and indirect effects. Second, though the absence of clouds was a major factor, a haze layer was essential to learn about haze impacts on radiation, although studying a pristine atmosphere would have been helpful in verifying the model. Third, a well-mixed boundary layer was imperative to ensure a thorough distribution of aerosol particles; i.e., there could be no nocturnal inversion. In practice, these constraints dictated that the most favorable times for collecting data were from about 0800 local time, after any nocturnal inversion had broken, until the first appearance of cumulus clouds.

Table 1.1. Instrumentation deployed and variables measured during the Rock Springs experiment.

Channel	Variable	Instrument
1	Temperature	Rotronics sensor
2	Relative humidity	Rotronics sensor
3	Pressure	Climatronics transducer
4	U-component of wind	Young propeller anemometer
5	V-component of wind	Young propeller anemometer
6	695-2800 nm flux	Eppley pyranometer
7	Instrument temperature	Eppley pyrgeometer
9	295-2800 nm flux	Eppley pyranometer
10	395-2800 nm flux	Eppley pyranometer
11	4000-50,000 nm flux	Eppley pyrgeometer
12	Ground temperature	Optitherm IR thermometer
13	Scattering coefficient	MRI nephelometer
14	Apparent sky temperature	Heimann pyrometer
15	Nephelometer temperature	MRI nephelometer

The last theoretical consideration was that of physically realistic assumptions. These were few but fundamental. Sulfate was judged to be anthropogenic because of the large industrial base of the northeastern United States. This assumption is important in that the experiment is designed to estimate man's impact on climate; however, from an atmospheric chemistry standpoint, the origin of the sulfate is irrelevant. Carbonaceous material was disregarded based on air sample analyses (Lamb, personal communication) done here. This

assumption is important because the aerosol is considered to have sulfate characteristics throughout this study. The scattering coefficient calculated at the surface was assumed constant throughout the boundary layer; this assumption ties directly in to a further assumption of a well-mixed boundary layer. The boundary layer is assumed to be well mixed because of the times of day chosen to take data, and is reasonable. The assumption of a constant scattering coefficient from the surface throughout the boundary layer is important. Since optical depth is proportional to k_{ext} , and k_{ext} is a function of height and wavelength, removing the height dependence enables $\tau(k_{\text{ext}}, dz)$ to be apportioned as a function of height more easily. The assumption would be very hard to prove experimentally, since measurements would have to be taken at many levels, but is plausible in a well-mixed boundary layer. The single-scatter albedo of sulfate aerosol particles was assumed to be unity (Hänel et al., 1980; Blanchet, 1989). That assumption itself is good, and can be justified by the finding that aerosol particles in this region are primarily sulfate.

Chapter 2

COMPARISON OF ROTATING SHADOWBAND RADIOMETER AND SUN PHOTOMETER OPTICAL DEPTH MEASUREMENTS

Before proceeding with the analysis of aerosol effects on the radiation budget, the relative merits of two different methods of measuring optical depth will be considered. Both a ten-channel sun photometer and a rotating shadowband radiometer (RSR) were deployed at Rock Springs. These two instruments both permitted the inference of optical depth from solar radiation data, but did so in different ways. Since the two devices measured the same quantity at the same time, a comparison of the relative correspondence of the data is worthwhile. If general accord is found, the reliability of each instrument is not only enhanced, but perhaps researchers can eliminate unnecessary redundancy in future work, saving time or money. If the results are at odds, further investigation is warranted into possible sources of error. It is beneficial at this point to review the physical processes and assumptions involved in the gathering of data by both the ten-channel photometer and the five-channel RSR, and to consider the merits and drawbacks of each.

The sun photometer used in this research was constructed at the University of Arizona. Its ten channels, ranging from 380 to 1029 nm, provide data from the near ultraviolet through the near infrared spectrum. Eight of the channels

were chosen to lie outside significant molecular absorption bands. The two channels selected to lie in weak absorption bands are the 670-nm channel, which experiences absorption by ozone, and the 939-nm channel, picked to estimate column water vapor concentration. The sun photometer consists of a tripod-mounted telescope, ten filters, and a photodiode. With the tripod aligned north-south, the telescope is aimed directly at the sun; the field of view under operating conditions is two degrees, meaning that only the direct component of sunlight is measured. The focused beam falls on a photodiode after passing through one of the filters; the filters on this instrument were computer-controlled, allowing the user to choose a period for each filter to be exposed in succession. When the beam passes through a given filter, the number of photons (which of course varies with wavelength) striking the photodiode excites the electrons thereon, producing a voltage. The total optical depth τ was then calculated using the formula

$$\tau = -\cos(\Theta_0) [\ln (V_\lambda/V_{0\lambda})] \quad (2.1)$$

where Θ_0 is the solar zenith angle, V_λ is the measured voltage, and $V_{0\lambda}$ is the zero-airmass calibration voltage, which is the voltage the sun photometer would yield if it were positioned at the top of the atmosphere. The zero-mass voltage is obtained using a procedure known as a Langley plot (except for the water vapor channel), and was last performed for this instrument in June-July 1993 at Mauna Loa Observatory, Hawaii. A summary of the sun photometer's channels and their respective zero-airmass calibration voltages can be found in Table 2.1.

Table 2.1. Wavelengths and corresponding zero-airmass calibration voltages of the Penn State sun photometer.

λ (nm)	$V_{0\lambda}$ (mV)
380	104.8
400	250.1
441	811.0
519	771.6
609	1400.0
670	950.9
780	1103.7
872	1376.7
939	-----
1029	911.9

The total optical depth is calculated in Equation 2.1. The Rayleigh component of the optical depth is determined (Goody, 1964) using the formula

$$\tau_R(p, \lambda) = \tau_{R0} (p_{sc}/1013.25) (\lambda_0/\lambda)^4 \quad (2.2)$$

where $\tau_R(p, \lambda)$ is the Rayleigh optical depth at a specified wavelength and pressure, τ_{R0} is the Rayleigh optical depth at 500 nm and 1013.25 mb (the value of τ_{R0} is 0.1447), p_{sc} is the surface pressure in millibars, λ_0 is 500 nm, and λ is the wavelength of interest in nm. The aerosol optical depth is then simply the difference of Equations 2.2 and 2.1, that is,

$$\tau_{aer} = \tau - \tau_R(p, \lambda) \quad (2.3)$$

where τ and $\tau_R(p, \lambda)$ are as defined in Equations 2.1 and 2.2.

The sun photometer provides many advantages in acquiring optical depths. It is a precision instrument capable of taking data at several wavelengths nearly simultaneously. The theory behind its photodiode is well-understood, and the calculations are straightforward. Also, since Rayleigh scattering is a known quantity, aerosol optical depth can readily be isolated. However, the photometer can be challenging to the user. It requires operator attention, partly because of a tendency to drift out of alignment, and partly because it can not be used in wet weather. Besides being fairly labor-intensive (with the associated costs), the photometer itself is expensive, costing about \$8000 (Michalsky et al., 1986). The bottom line is that the sun photometer allows precise but costly readings.

The expense of the sun photometer has prompted a search for a reliable but cheaper method of gaining radiation data. The rotating shadowband radiometer (RSR) is a possible solution. Unlike the sun photometer, the RSR theoretically requires almost no supervision or maintenance. Michalsky et al. (1986) have claimed that a RSR can be built for \$1500 and provide optical depth data as accurate as those from a sun photometer.

The rotating shadowband radiometer operates very differently from the sun photometer. Whereas the sun photometer measures the direct solar beam, the RSR infers the value indirectly. There are three components of solar radiation (Michalsky et al., 1986): the direct normal, which is measured by the sun photometer; the diffuse horizontal, which is the light detected when the sun is blocked; and the total horizontal, which is the sum of direct and diffuse. Since

there are three components, of which one is simply the sum of the other two, it stands to reason that if any two of these values are known, the third can easily be obtained. From this simple but useful fact arose the shadowband radiometer. The device (Michalsky et al., 1986) consists of a mount, which must be properly aligned before using (but theoretically never again), a silicon-based sensor, and a shadowband, eight degrees wide, which is motor-controlled. The constant-speed motor drives the shadowband, periodically shading the sensor. When the band is not shading the pyranometer, the total solar radiation is impinging on the sensor; when the band is shading the pyranometer, only diffuse radiation strikes the sensor. Since the total horizontal and diffuse radiation are known quantities, their difference can be deduced to be the direct beam, from which optical depth can be inferred. The RSR used in this experiment (Michalsky et al., 1986) is equipped with a microprocessor to correct for sensor temperature and cosine and spectral effects. It measures optical depths at five wavelengths (415 nm, 500 nm, 610 nm, 665 nm, and 862 nm), and can take up to 240 measurements per hour.

The rotating shadowband radiometer has many favorable attributes. It can be used in all weather, demands almost no maintenance, and, at an initial cost of \$1500, represents a considerable savings when compared with the photometer. The savings increase with time, as there are virtually no labor costs involved with a RSR. For all its benefits, however, the RSR does have weaknesses. Diffuse radiation data (Michalsky, personal communication) may have errors as large as twenty percent on the open silicon channel, though no such problem exists for

the five aerosol channels. Also, some scattered light that strikes the eight-degree field of view (FOV) of the RSR sensor (Michalsky, personal communication) is not seen by the two-degree FOV of the photometer, leading to excessive "direct" radiation and falsely low optical depth values given by the RSR. The RSR is a cheap alternative to a sun photometer, but may lack the latter's precision.

Comparing the data from the sun photometer and the rotating shadowband radiometer will permit an analysis of the consistency of the instruments with each other. Figure 2.1 is a scatter plot of the RSR aerosol optical depth at 415 nm versus the sun photometer aerosol optical depth at 400 nm. Data were chosen during periods when solar flux was steadily changing, indicating an absence of clouds. The periods range from one to three hours in length. Figure 2.1 shows that the sun photometer data nearly always have higher values than those from the RSR. This is expected; the RSR shadow is too large and underestimates the diffuse field. Since the total beam is the direct plus the diffuse, the measured direct beam is thus too large, and lower values of optical depth from the RSR result. Figures 2.2-2.5 show better consistency than is seen in Figure 2.1; agreement generally improves with increasing wavelength. The large deviations on August 23 may be due to the sun photometer being slightly out of alignment. The radiometer's wider FOV lets diffuse radiation into the direct field. Diffuse radiation is greater at shorter wavelengths due to molecular scattering; it is possible that a similar relation is true for aerosol scattering. The RSR would agree better with the sun photometer at longer wavelengths.

Optical Depth Comparison

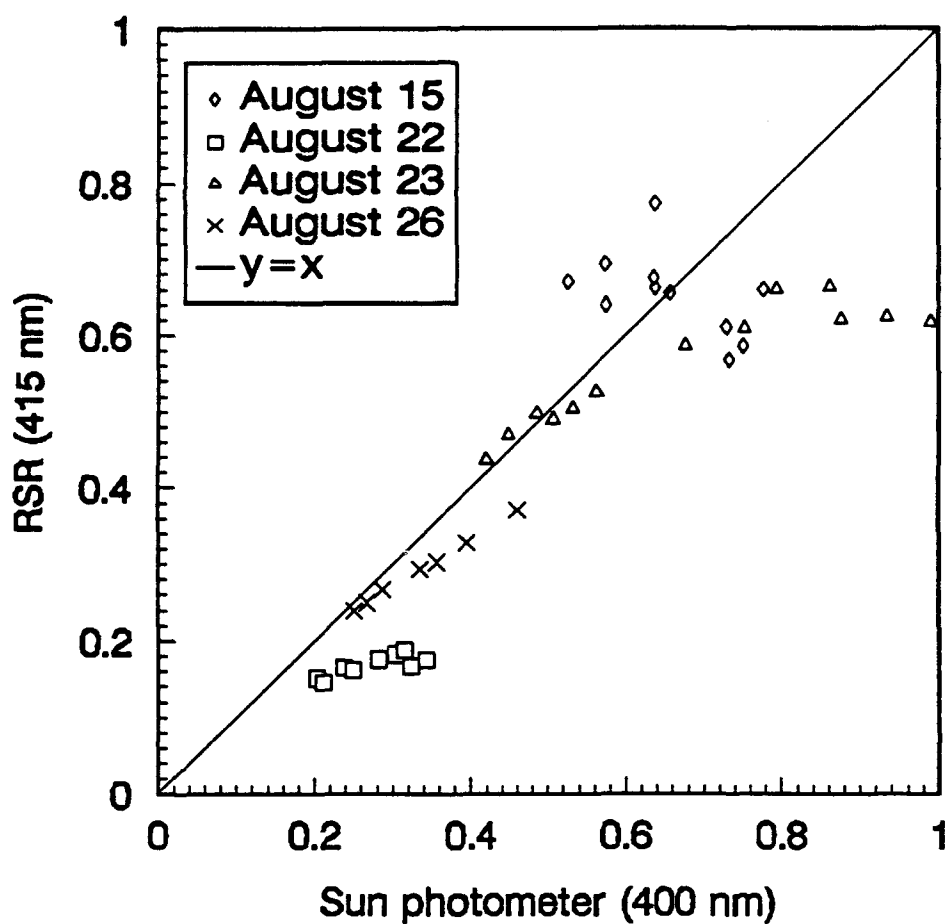


Figure 2.1. Scatter plot of optical depth data obtained by RSR at 415 nm versus those acquired by sun photometer at 400 nm. Each point denotes a ten-minute optical depth average.

Optical Depth Comparison

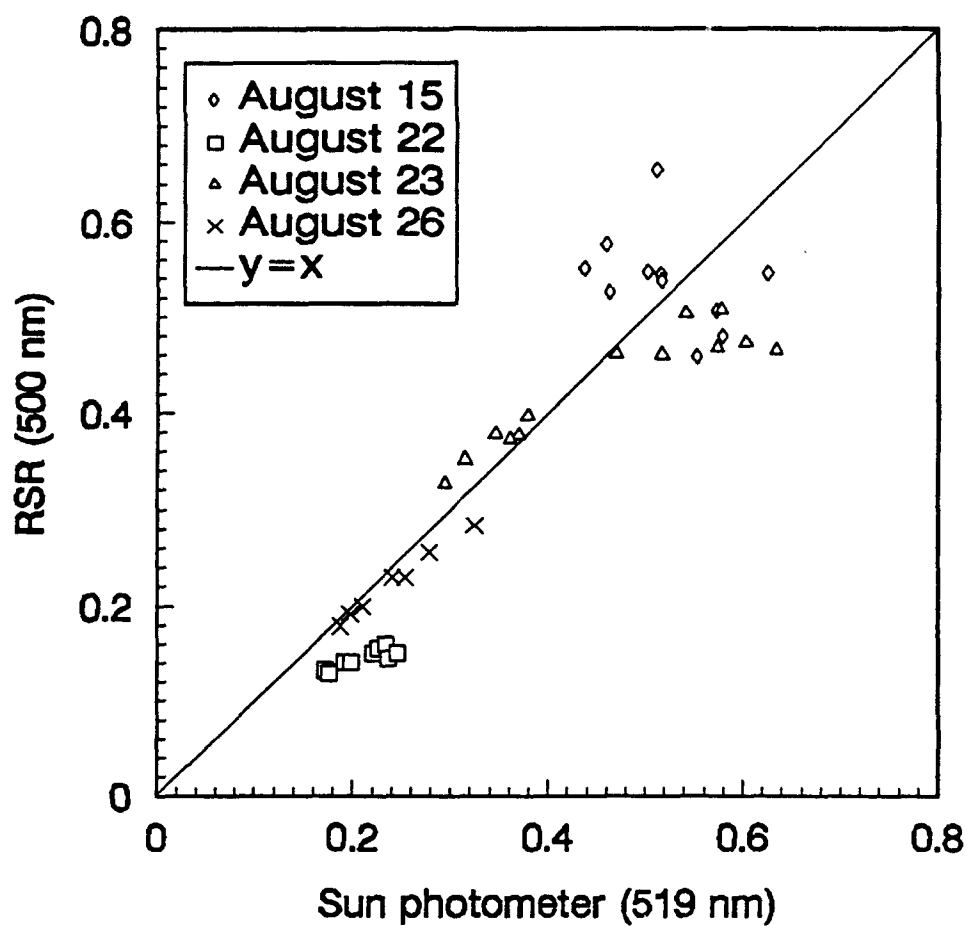


Figure 2.2. Same as in Figure 2.1, but with wavelengths of 500 nm versus 519 nm.

Optical Depth Comparison

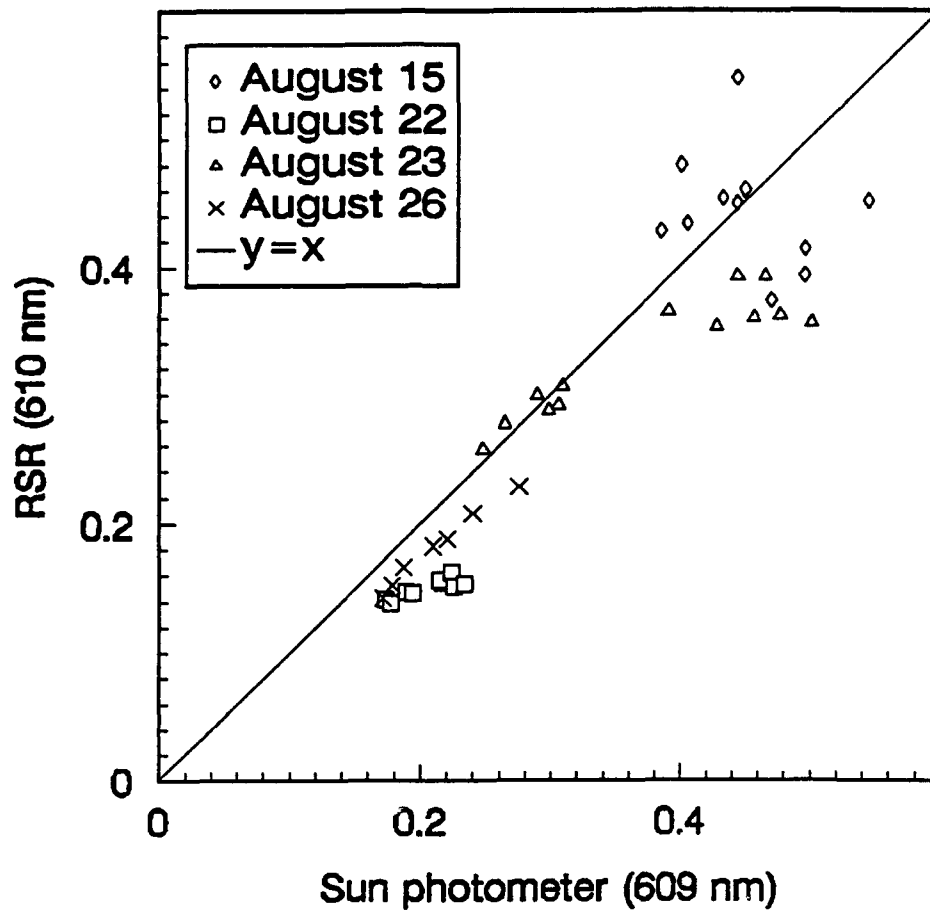


Figure 2.3. Same as in Figure 2.1, but with wavelengths of 610 nm versus 609 nm.

Optical Depth Comparison

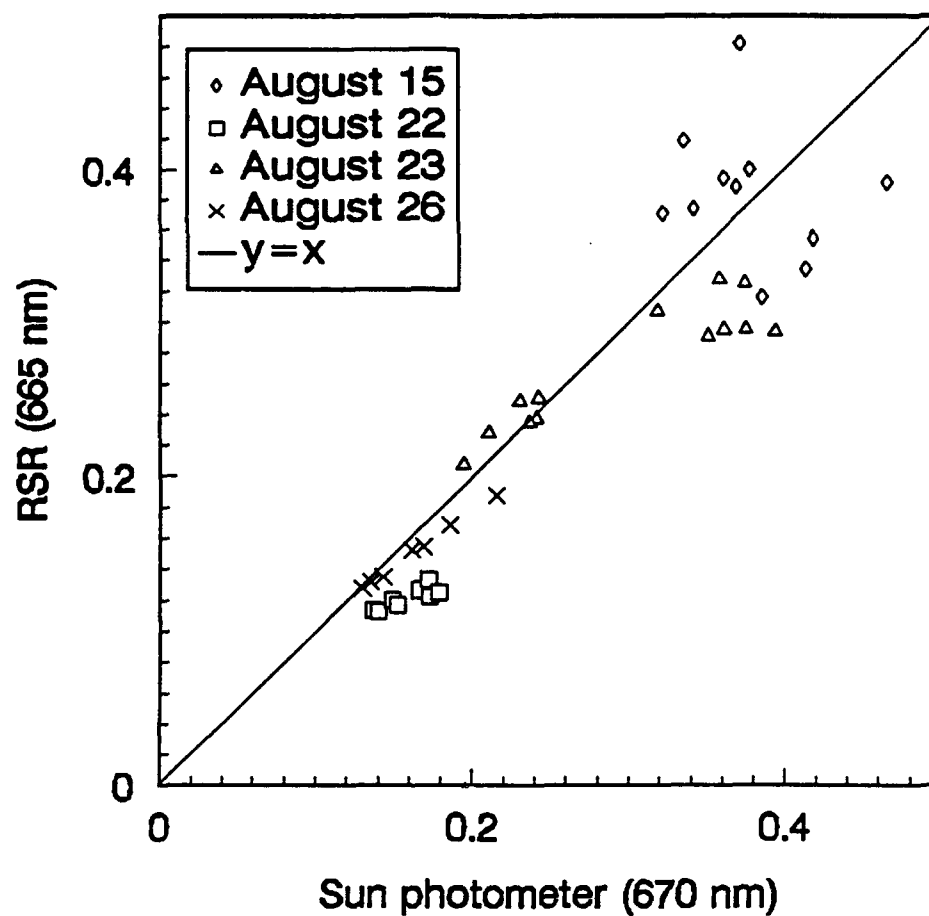


Figure 2.4. Same as in Figure 2.1, but with wavelengths of 665 nm versus 670 nm.

Optical Depth Comparison

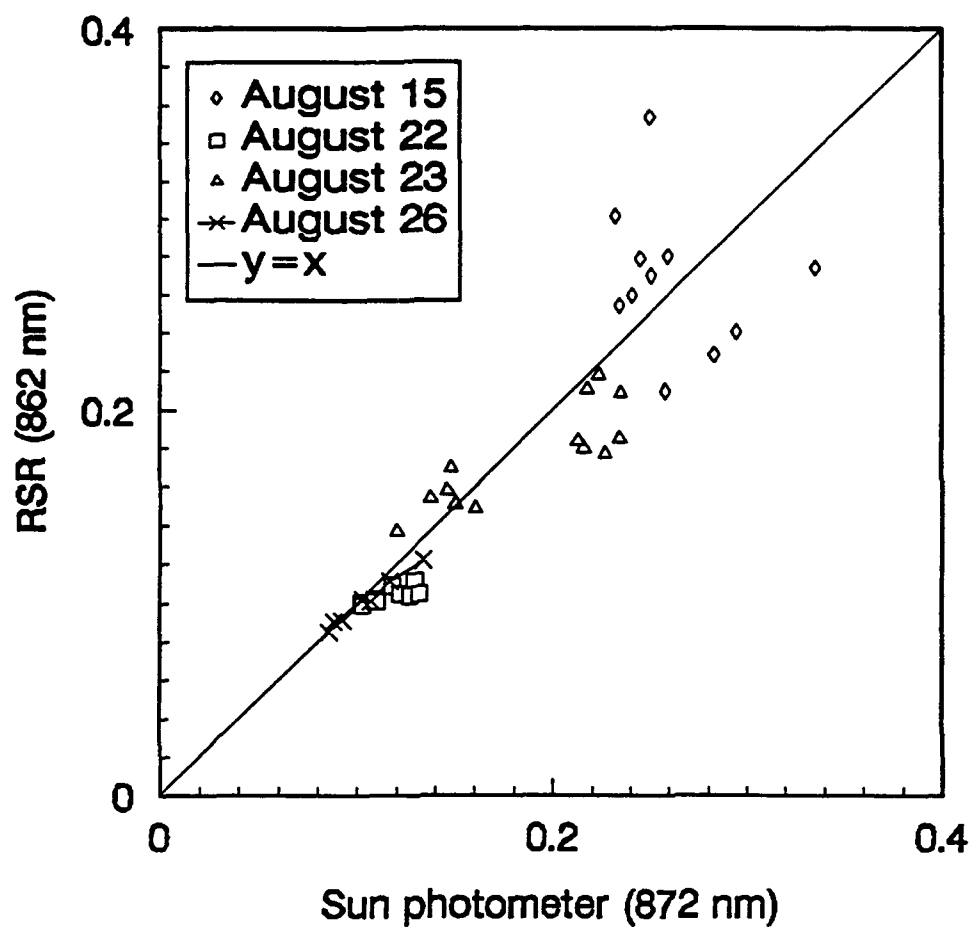


Figure 2.5. Same as in Figure 2.1, but with wavelengths of 862 nm versus 872 nm.

A different perspective can be gained on the data by averaging all points at a given wavelength during a single observational period. This allows an examination of the variability of the data, construction of a best-fit curve, and calculation of a correlation coefficient for the data. From Figures 2.6-2.10, which contain all of the data in Figures 2.1-2.5 in more compact form, some interesting observations can be made. First, at no wavelength are there glaring differences; the weakest agreement (Figure 2.6) is relatively robust. Second, the data in Figure 2.6 show the smallest consensus between the RSR and sun photometer, and the best accord occurs in Figure 2.10, at the longest wavelengths. Third, forcing all of the equations to have the standard form of a line with a y-intercept of zero, i.e., $y = mx$, always results in a slope value of less than one. Since this shows that the RSR optical depth values are on average lower than those acquired by the sun photometer, it was decided to take another approach to the problem: determine if an offset exists between the data sets, and, if so, attempt to quantify it as a function of wavelength.

The first approach was simply to fit the curves again, but this time fitting an intercept as well as a slope. After doing this, though, it was clear that the intercept was merely an unreliable artifact of curve-fitting, because all curves now had a slope greater than one. To get a good idea of the true offset, the average differences ($\Delta\tau$) of each of the four sets of optical depth data (sun photometer minus RSR values to yield positive answers) were plotted as a function of wavelength (Figure 2.11).

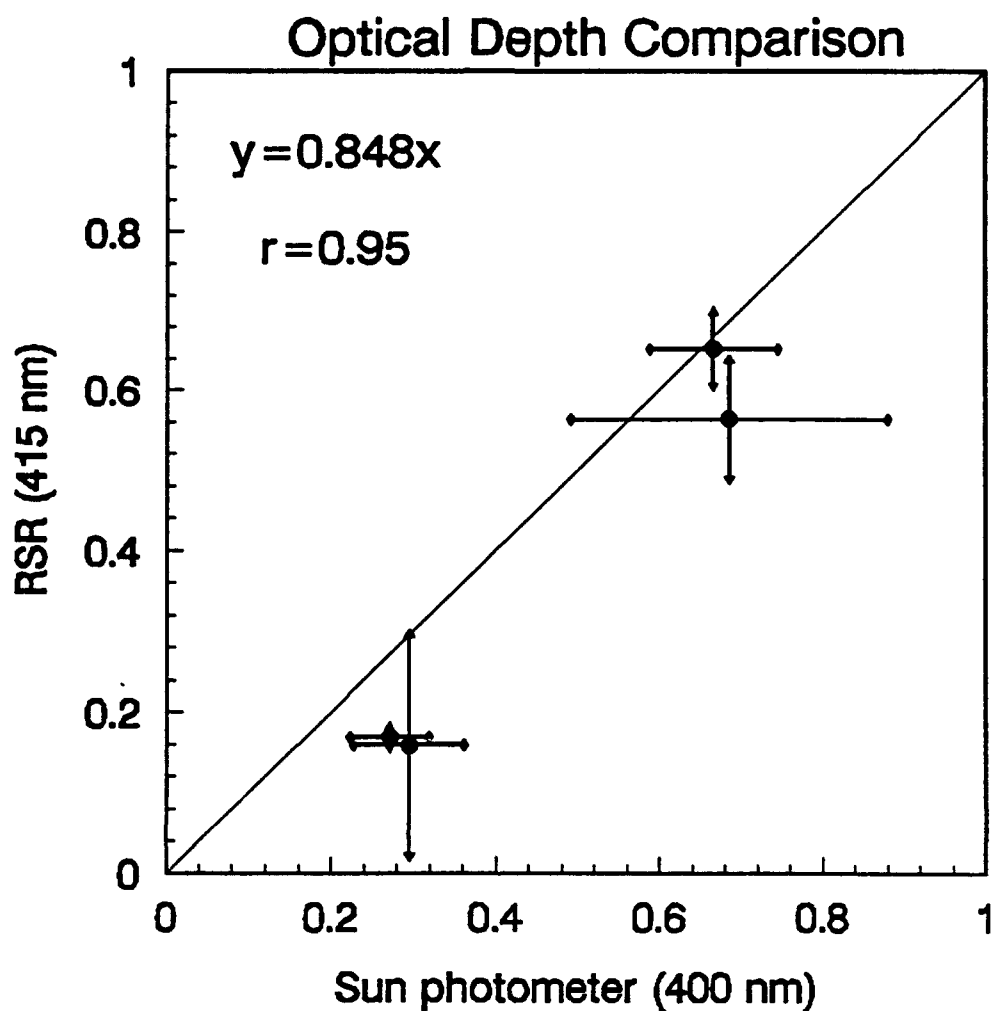


Figure 2.6. Scatter plot of RSR optical depth data gathered at 415 nm versus those acquired by sun photometer at 400 nm. Each point represents data averaged for an entire day; periods range from one to three hours. Vertical and horizontal error bars represent standard deviations of RSR and sun photometer data, respectively. Best-fit equation (linear regression with y-intercept forced to zero) and correlation coefficient are shown at upper left. The line shows the perfect fit of $y = x$.

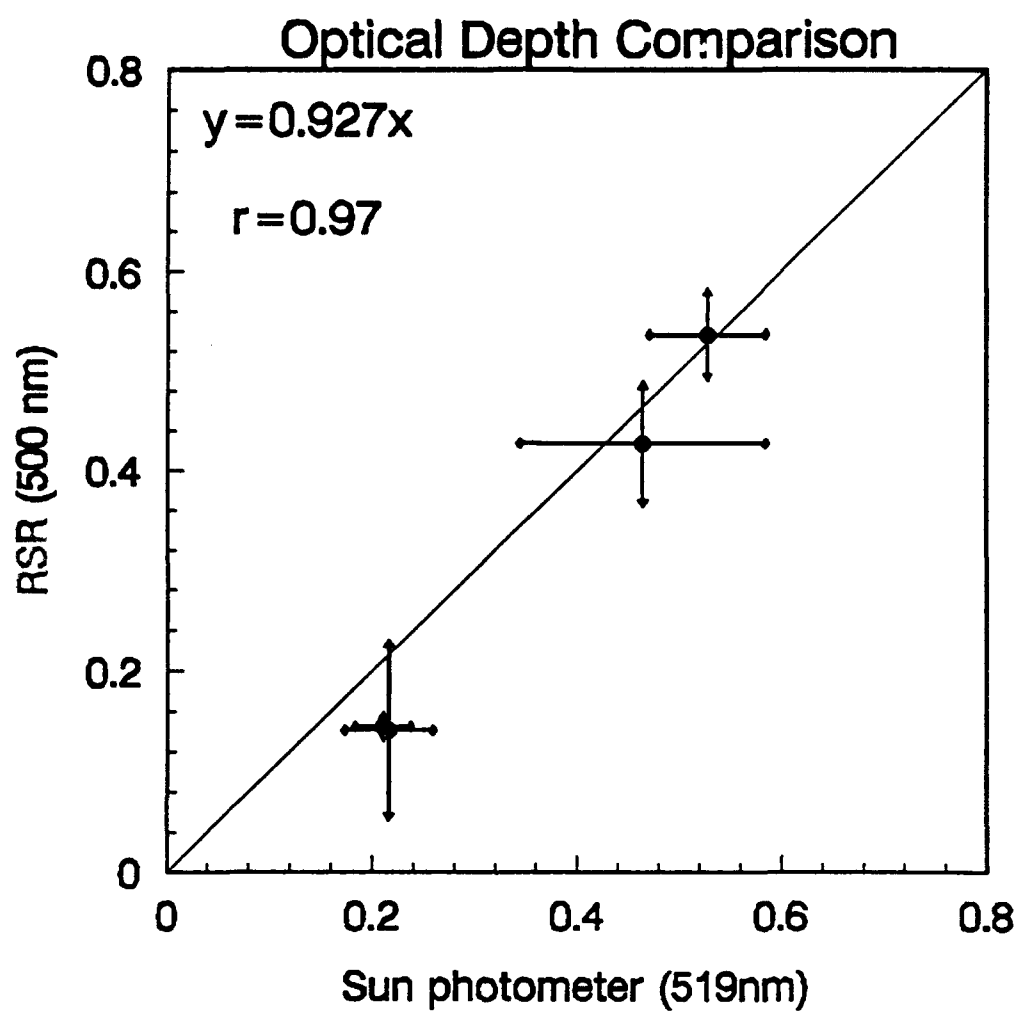


Figure 2.7. Same as in Figure 2.6, but with wavelengths of 500 nm versus 519 nm.

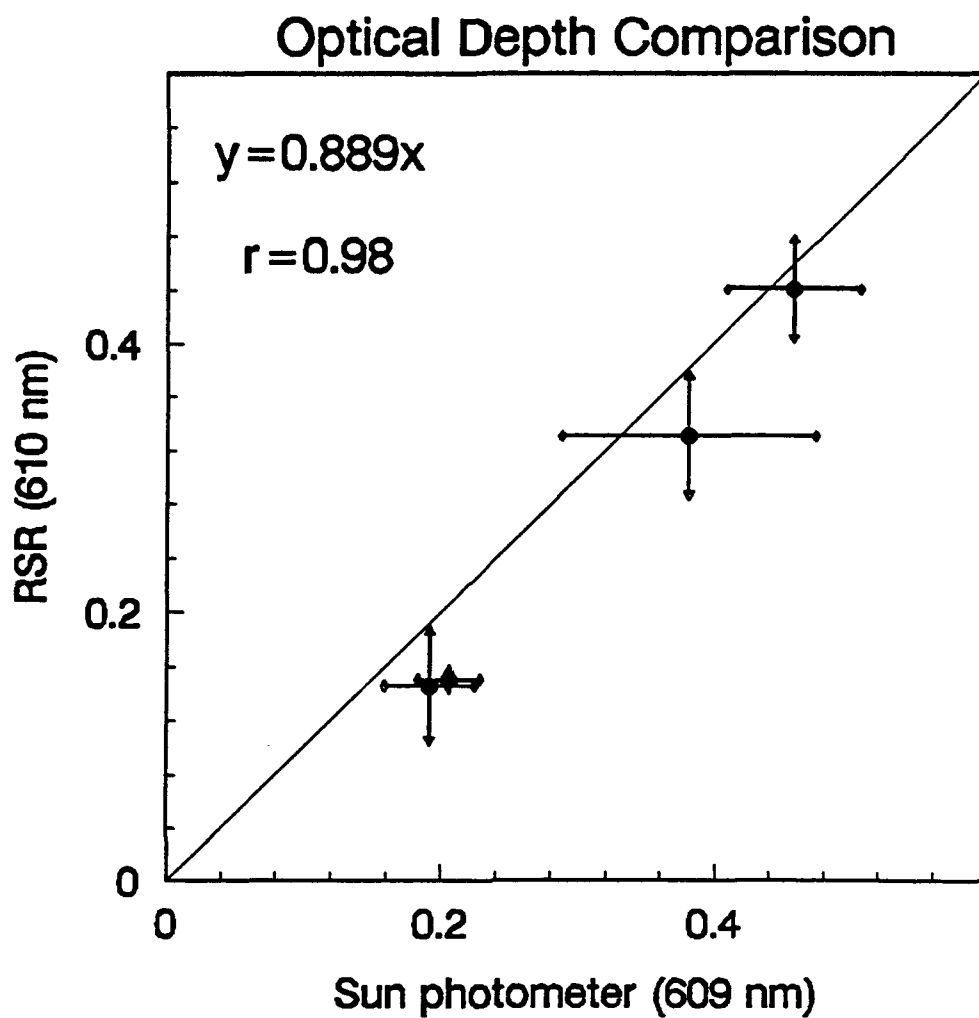


Figure 2.8. Same as in Figure 2.6, but with wavelengths of 610 nm versus 609 nm.

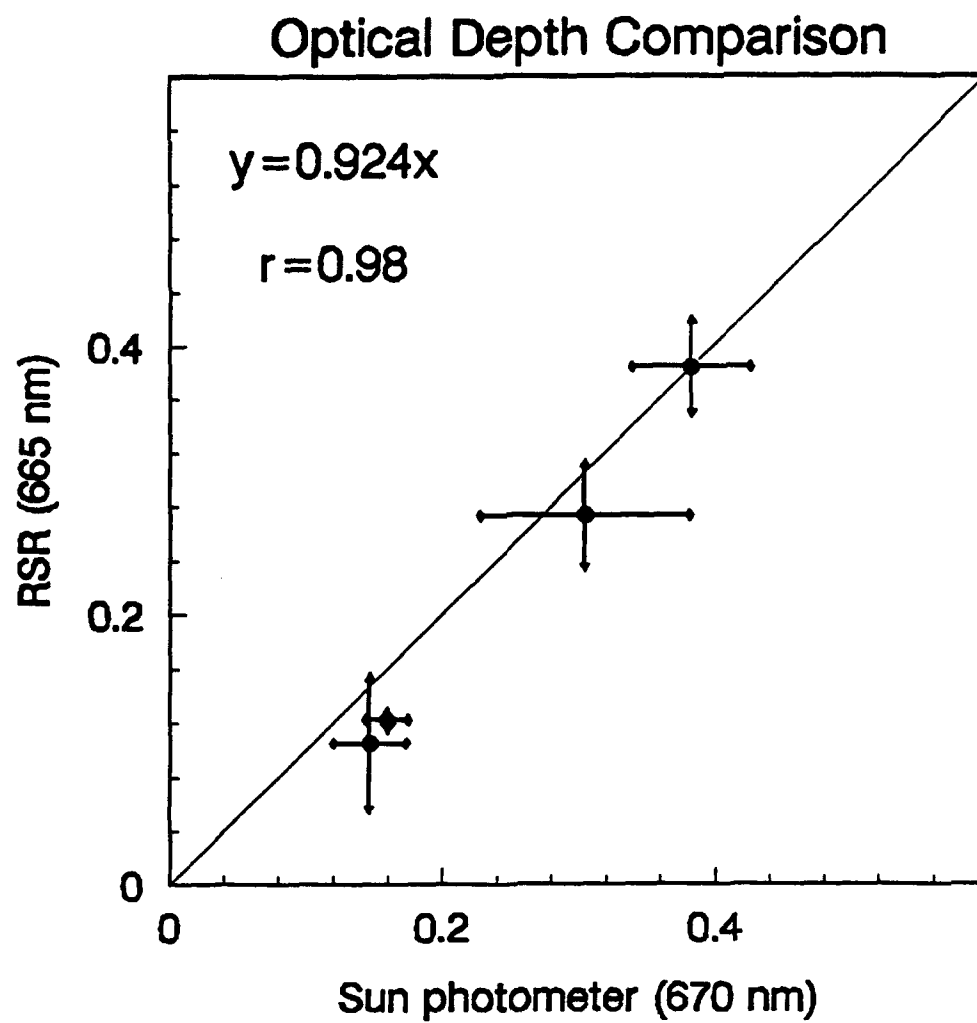


Figure 2.9. Same as in Figure 2.6, but with wavelengths of 665 nm versus 670 nm.

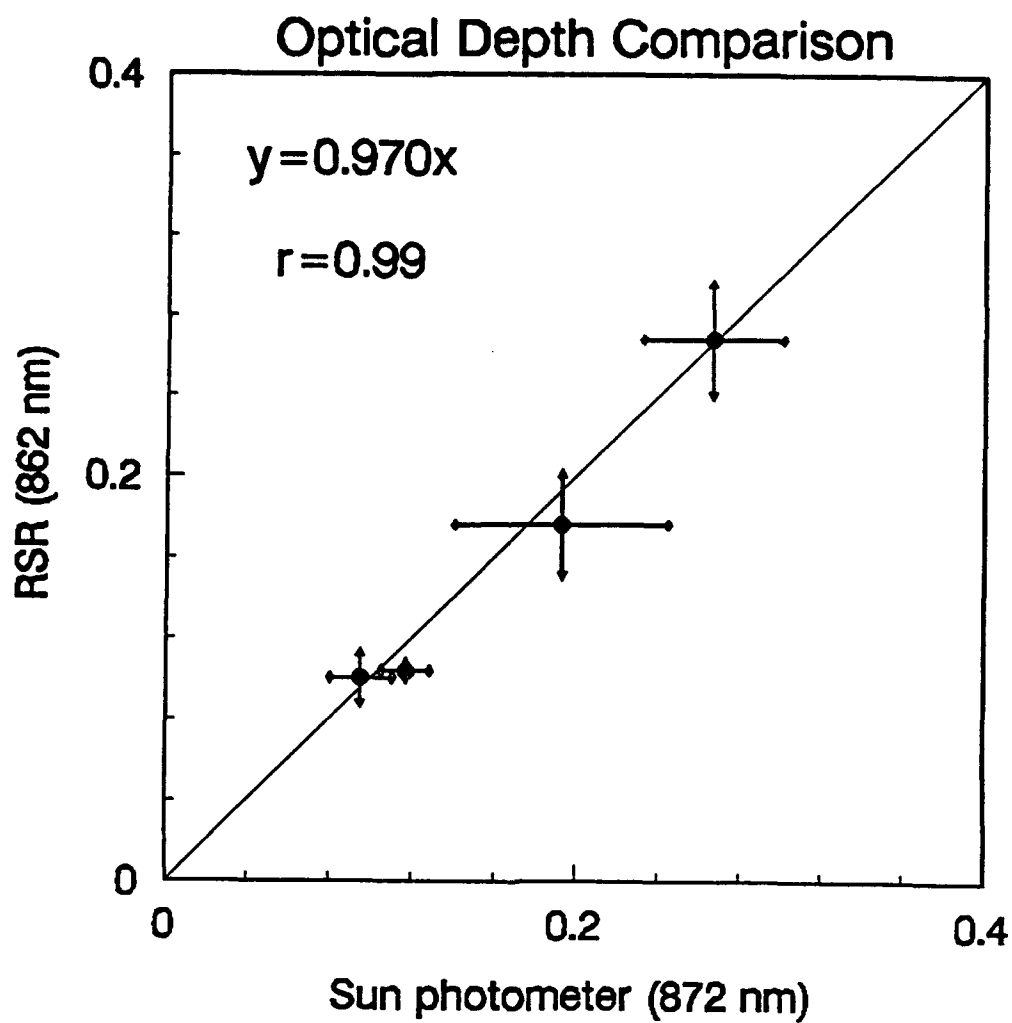


Figure 2.10. Same as in Figure 2.6, but with wavelengths of 862 nm versus 872 nm.

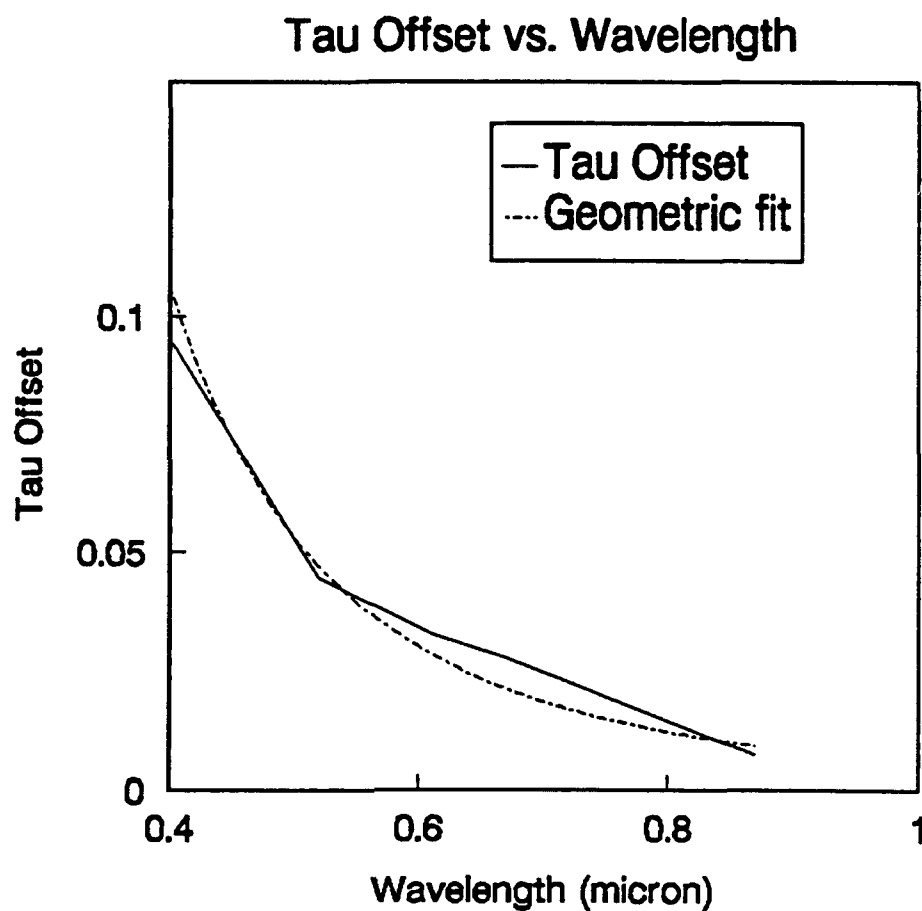


Figure 2.11. Optical depth offset between sun photometer and RSR. The data curve is shown together with a best-fit curve, which shows a relationship between $\Delta\tau$ and λ similar to that between scattering and wavelength. The equation of the best-fit curve is $\Delta\tau = (6.19 \times 10^{-3})\lambda^{-3.1}$.

The curves show that the offset decreases geometrically with increasing wavelength. In trying to determine why such a relationship would exist, various factors were taken into account, bearing in mind that the RSR's eight-degree field of view was likely to be a key. The RSR values of optical depth are falsely low. Direct radiation is the difference between total and diffuse flux, and the shadowband obscures too much diffuse radiation during the periods when the sensor is shaded. The result is too high a value of direct radiation, which in turn implies a lower optical depth. It seemed plausible that the amount of diffuse radiation would increase strongly with decreasing wavelength. There is more diffuse radiation at shorter wavelengths due to molecular scattering, and possibly more due to aerosol scattering as well. The error in the inferred direct radiation value (and thus the optical depth) given by the RSR would range from very significant at short wavelengths to negligible at longer ones.

After fitting a curve to the data in Figure 2.11, it was found to be governed by the equation

$$\tau_{SP} = \tau_{RSR} + (6.19 \times 10^{-3}) \lambda^{-3.1}, \quad (2.4)$$

where the subscripts indicate the instrument used. Equation 2.4 displays some similarity to the λ^{-4} relationship between wavelength and molecular scattering. From the evidence above, the RSR is a suitable (or preferable) alternative to the sun photometer. The RSR is much less expensive to deploy and operate than a sun photometer, which is a significant argument in its favor. Additionally, though the rotating shadowband radiometer is known to be less precise than the

sun photometer, it appears that its error is predictable and can be corrected (this would certainly need to be confirmed with further experiments). Use of the RSR would result in measurements as precise as those of the sun photometer (after allowances are made at each wavelength for excess diffuse radiation) at considerably less cost. For the remainder of this work, the sun photometer's measurements, which require no corrections, will be used to estimate aerosol effects on the surface radiation budget.

Chapter 3

CALCULATION OF SURFACE INSOLATION

The purpose of this study is to determine the extent to which sulfate haze attenuates incoming solar radiation, and to learn whether visibility and/or relative humidity correlates well with changes in insolation. The sulfate-induced effects on the surface radiation are calculated by using observed meteorological properties as input for an atmospheric radiative transfer model. To test the model, it is first run with the observed aerosol loading and its output compared with the solar flux values obtained at Rock Springs. When a strong correlation is found, the model is run with no aerosol loading, and the haze effect deduced to be simply the difference between the computer output with and without aerosol. If a strong relationship is discovered between the haze effect and visibility, the further aim to provide climate modelers with a simple parameterization of sulfate haze may be facilitated, since visibility is a commonly measured variable.

To realize the goals above, several preliminary calculations were required. As cited in Chapter 1, many instruments were deployed to allow measurement of all parameters relevant to radiative transfer calculations. These included a nephelometer to measure scattering coefficient at the surface, a microwave radiometer to measure water vapor content, a ceilometer to estimate boundary

layer height, radiosonde launches to measure the vertical profile of the atmosphere, and the instruments enumerated in Table 1.1 to measure surface variables. At this point it is worthwhile to discuss the intermediate parameters needed to run the radiative transfer model, the processes used to obtain them, and the assumptions made about each; this will be followed by a description of the model itself.

To calculate aerosol optical depth, one of the most elementary equations in radiative transfer is used (Twomey, 1977):

$$\tau(\lambda) = \int_0^z k_{\text{ext}}(\lambda, z) dz \quad (3.1)$$

where $\tau(\lambda)$ is the total optical depth, $k_{\text{ext}}(\lambda, z)$ is the extinction coefficient of the medium, and dz is the distance traveled by the beam through the medium. Equation 3.1, while a powerful general statement, could not easily be applied to this research; each of its three terms is problematic in the form shown. The important variables for this study are the aerosol optical depth, not the total optical depth; the extinction coefficient could not be measured accurately; dz needs to be clearly defined. The first simplification made was to subtract the Rayleigh component τ_{Ray} , a well-known wavelength-dependent quantity, as shown in Equation 2.3. Another key assumption, noted in Chapter 1, is that k_{ext} is approximately equal to k_{scat} ; the supposition is based upon work by Hänel (1980), who stated that sulfate aerosols have a single-scattering albedo close to one, and

by Lamb (personal communication), whose analysis of central Pennsylvania air samples indicates sulfate to be the principal aerosol component. Finally, dz is fixed as the height of the boundary layer on the grounds that aerosol is predominantly present only in the boundary layer and thus affects sunlight only in the lowest few kilometers. Though all of these assumptions expedited research into aerosol optical depth, some of the instrumentation failed to yield results accurate enough for this experiment.

3.1. Boundary layer extent.

If both k_{scat} and the boundary layer height were known, Equation 3.1 would provide a third means of estimating optical depth (after the sun photometer and RSR). Before this experiment began, it was hoped that a lidar could be used to measure the boundary layer height, but the instrument was not funded. As a result, a laser-beam ceilometer already in place was designated a suitable alternative. Unfortunately, the ceilometer return lacked the sensitivity necessary to supply any information about the height of the boundary layer. Having launched radiosondes regularly, the last recourse was to estimate the vertical extent of the boundary layer at the time of launch based on the sonde data. While this method fails to provide any details as to the temporal evolution of the boundary layer, it does yield a relatively accurate first-order approximation of its bounds at a given time. Also, since launches occurred during the middle of

taking data, and since the boundary layer was already well-mixed, the estimate, while imprecise, should result in the minimal error possible under the circumstances. The boundary layer heights estimated during this experiment ranged from 1200-1800 m above sea level (the site elevation is 375 m).

3.2. Scattering coefficient.

An integrating nephelometer and recorder manufactured by Meteorology Research inc. (MRI) was deployed to gather visibility and scattering coefficient data. The instrument is designed to make continuous measurements of the volume scattering coefficient; i.e., $k_{\text{scat}} + k_{\text{Ray}}$, where k_{scat} is approximately equal to k_{ext} in Equation 3.1, and k_{Ray} is the Rayleigh scattering coefficient. The air quality is determined by taking into account k_{scat} while disregarding k_{Ray} . Additionally, the MRI nephelometer is equipped with a manually-controlled heater to be used when ambient relative humidity exceeds 65%; the heater reduces the relative humidity of the sampled air to less than 60% to ensure that scattering due to pollutants, not water droplets, is measured. The nephelometer is built to measure scattering coefficient, from which visibility and mass concentration of particulate matter are inferred. Its effective ranges for these three variables are 0.01 to 0.1 m^{-1} , 500 m to ∞ , and 0 to 3800 μgm^{-3} , respectively.

In practice, the nephelometer proved inadequate to measure visibility or scattering coefficient to any degree of accuracy. Therefore, estimating optical

depth (as a check against the sun photometer and RSR) using Equation 3.1 and ceilometer and nephelometer data was no longer viable. The nephelometer tended to become contaminated quickly by cobwebs and soil in the rural environment; this was not entirely unexpected given the dusty conditions exacerbated by occasional fieldwork adjacent to the nephelometer site. Under these conditions the nephelometer readings could not be considered reliable.

Since visibility and scattering coefficient are still important, it was decided to rely on the sun photometer readings and the estimated boundary layer height, and compute the scattering coefficient by inverting Equation 3.1; that is:

$$k_{\text{ext}} = k_{\text{scat}} = \tau/dz \quad (3.2)$$

where all variables are as defined in Equation 3.1. Though optical depth values are assumed to be precise, dz is subject to sizable uncertainty, and the scattering coefficient derived in this way will likely also have a large error.

3.3. Relative humidity profile.

The relative humidity profile is vitally important to this work. The total water vapor and its dispersion are vital in determining the aerosol size distribution, which in turn has a large bearing on the aerosol optical depth. The instruments used to find the water vapor profile proved reliable. A microwave radiometer was used to learn the total columnar water vapor content; radiosondes were launched to determine the water vapor distribution as a

function of height. A bonus of using both the radiometer and radiosondes was that the integrated water vapor could be verified by adding the amounts in each atmospheric layer as partitioned by a model, and comparing with the radiometer output (averaged over the period studied on a given day). The results given by the two methods showed good accord (Figure 3.1), not surprising since the radiometer was calibrated using both radiosondes and tipping curves. Since the study was to be done under cloud-free skies, the radiometer, which also measures integrated liquid water, was used to check for liquid water clouds. Liquid water denoted clouds (except cirrus) and those data were ignored. All data here were taken during times of zero liquid water content as measured by the radiometer.

3.4. Vertical aerosol distribution.

Taking the radiosonde data and partitioning water vapor into vertical bins provides only half of the information necessary to construct a vertical aerosol distribution; the profile of the aerosol particles themselves as well as that of the water vapor is required. There are at least a couple of ways to proceed in mathematically representing the vertical distribution of aerosol. Given optical depth data, King et al. (1978) inverted the measurements as a function of wavelength to yield a Junge distribution (Junge, 1963). The size distribution and aerosol optical depth as a function of wavelength are related (King et al., 1978) through the expression:

Water Vapor Content Comparison

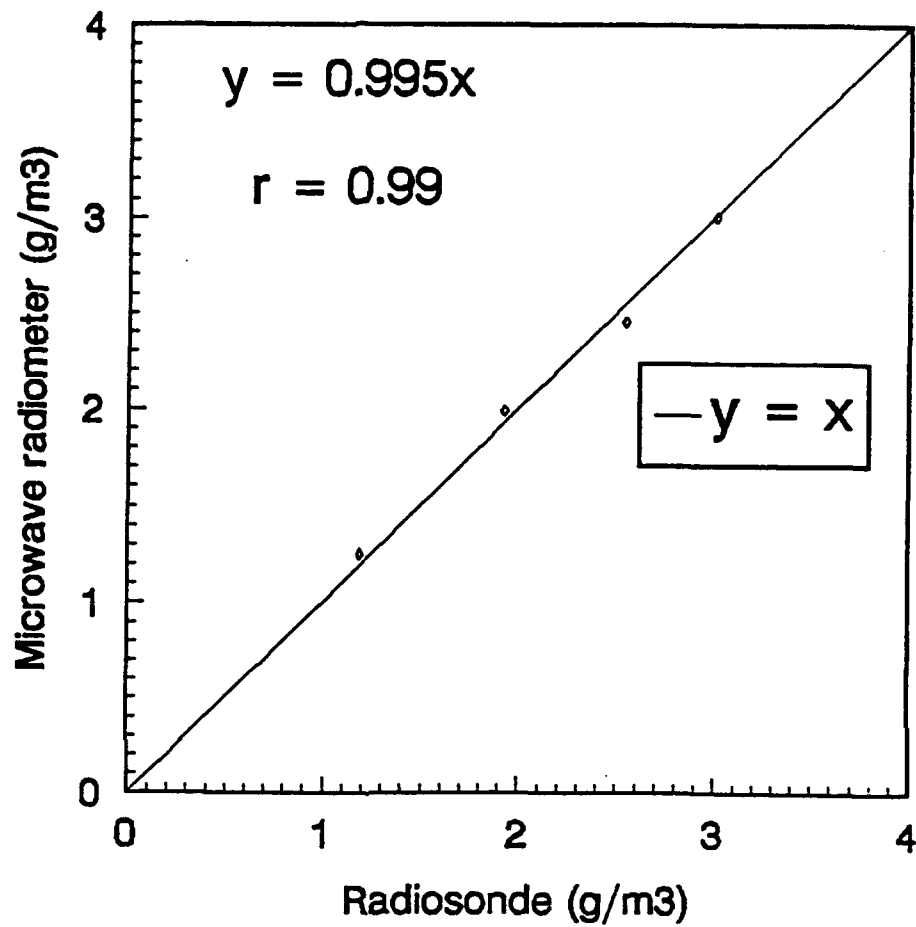


Figure 3.1. Scatter plot of water vapor content as measured by radiosonde versus that evaluated (averaged over the period in question) by the microwave radiometer. Best-fit equation and correlation coefficient are at upper left.

$$\tau_{\text{aer}}(\lambda) = \int_0^{\infty} \int_0^{\infty} \pi r^2 Q_{\text{ext}}(r, \lambda, m) n(r, z) dz dr, \quad (3.3)$$

where $\tau_{\text{aer}}(\lambda)$ is the wavelength-dependent aerosol optical depth, Q_{ext} is the extinction efficiency factor from Mie theory, λ is the wavelength of the incident radiation, $n(r, z)$ is the height-dependent aerosol number density in the radius range r to $r + dr$, and m is the complex refractive index of the aerosol particles (a complete list of complex refractive indices for sulfate and other particles at wavelengths from 0.300-4.000 μm may be found in d'Almeida et al., 1991).

The result of evaluating the height integral in Equation 3.3 is (King et al., 1978):

$$\tau_{\text{aer}}(\lambda) = \int_0^{\infty} \pi r^2 Q_{\text{ext}}(r, \lambda, m) n_c(r) dr, \quad (3.4)$$

where $n_c(r)$ is the columnar aerosol size distribution, i.e., the number of particles per unit area in a given radius interval in a vertical column. Integration is only to the top of the boundary layer, not (as King) to the "top of the atmosphere."

To determine $n_c(r)$ (King et al., 1978), the transform of Equation 3.4 must be obtained; however, since an expression for $n_c(r)$ can not be written analytically as a function of $\tau_{\text{aer}}(\lambda)$, the integral in Equation 3.4 must be approximated. This is accomplished by using a summation over coarse intervals in r , each of which is composed of several finer subintervals as described by Herman et al. (1971) for the case of the angular distribution of scattered monochromatic light. To examine the specific kernel functions which result when the procedure above is

applied (King et al., 1978), $n_c(r)$ is set equal to $h(r)f(r)$, where $h(r)$ is a rapidly varying function of r and $f(r)$ varies slowly. With this substitution, Equation 3.4 becomes:

$$\tau_{\text{ser}}(\lambda) = \int_{r_a}^{r_b} \pi r^2 Q_{\text{ext}}(r, \lambda, m) h(r) f(r) dr, \quad (3.5)$$

where the limits of integration have been made finite and range from r_a to r_b .

Equation 3.5 can then be approximated as a summation; i.e.:

$$\tau_{\text{ser}}(\lambda) = \sum_{j=1}^n \int_{r_j}^{r_{j+1}} \pi r^2 Q_{\text{ext}}(r, \lambda, m) h(r) f(r) dr, \quad (3.6)$$

where $r_1 = r_a$ and $r_{n+1} = r_b$.

Using Equation 3.6, King et al. (1978) assumed $f(r)$, which varies slowly, as constant in each coarse interval, which resulted in a system of linear equations they represented as the vector equation:

$$g = Af + e \quad (3.7)$$

where g represents the measured quantity, Af signifies the theoretical solution, and e is an unknown error vector which represents the deviation between theory and measurement. The discrepancy e arises from quadrature and measurement errors and from uncertainties as to the exact form of the kernel function (in this case, $\pi r^2 Q_{\text{ext}}(r, \lambda, m)$).

It follows (King et al., 1978) from Equation 3.6 that the elements of Equation 3.7 are given by:

$$g_i = \tau_{\text{ext}}(\lambda_i), \quad i = 1, 2, \dots, p,$$

$$A_{ij} = \int_{r_j}^{r_{j+1}} \pi r^2 Q_{\text{ext}}(r, \lambda_i, m) h(r) dr, \quad j = 1, 2, \dots, n, \quad (3.8)$$

$$f_j = f(\bar{r}_j),$$

where (\bar{r}_j) are the midpoints of the coarse intervals.

In terms of an integral over $x = \log r$, Equation 3.8 may be rewritten (King et al., 1978) as:

$$A_{ij} = \int_{x_j}^{x_{j+1}} K(x, \lambda_i) dx, \quad (3.9)$$

where

$$K(x, \lambda) = \pi 10^{3x} Q_{\text{ext}}(10^x, \lambda, m) h(10^x) \ln 10. \quad (3.10)$$

Equations 3.9 and 3.10 are the same as those obtained by Yamamoto and Tanaka (1969) if $h(r)$ takes the form of a Junge distribution, i.e.,

$$h(r) = r^{-(\nu^*+1)} \quad (3.11)$$

with the Junge parameter ν^* assumed to have a value of 3.0.

Despite the utility of the above equations, the assumption of a Junge distribution has been found to be problematic by King et al. (1978), who noted that the distribution is almost a delta function for large values of ν^* (on a linear scale), and by Davies (1974), who pointed out that the Junge power law is independent of larger particles and thus can not be applied to aerosols. In addition, experiments done by King et al. (1978) in which aerosol size

distributions were obtained by inverting optical depth measurements, showed clearly that a Junge distribution occurred on only about twenty percent of the days during which measurements were taken. Finally, King et al. (1978) pointed out that due to the extinction cross-sections (which increase rapidly with radius), and number densities of aerosol particles (which normally decrease with radius), measurements of attenuation in the solar spectrum limits the radius range of maximum sensitivity to large and giant particles only (0.1-4.0 μm). Since there is no strict rule as to which radii range contributes most strongly to attenuation, particles below 0.1 μm in diameter, which have much higher number densities than larger particles, and those larger than 4.0 μm , which have much higher extinction coefficients, must be adequately represented.

To address the problem of accurately depicting aerosols in the atmosphere, Davies (1974) advanced the use of a log-normal distribution. He began with the standard Junge (1963) distribution equation:

$$dN/d\ln r = cr^{-\beta}, \quad (3.12)$$

where dN is the number of particles per cm^3 in the range $d\ln r$, N is the total number of particles per cm^3 , c is a constant depending on the total number, and β is claimed by Junge and Jaenicke (1971) to be approximately three for radii less than 10 μm , and near six for radii greater than 10 μm . Davies (1974) proved that if Equation 3.12 is used, particles of size 0.1-1.0 μm are those primarily represented; adding particles of radii 1-10 μm has only a slight effect on the expression, and adding particles of size 10-100 μm has no effect. Using several

values of β , Davies (1974) showed the minimal effect of large particles ($> 10\mu\text{m}$) on a Junge distribution (Table 3.1) and its weakness in representing aerosols.

As a solution to the aerosol dispersion problem, Davies (1974) proposed that a log-normal distribution would represent aerosols well based on work with Los Angeles smog particles. Davies (1974) began with the basic log-normal equation:

$$\frac{dN}{d\ln r} = \frac{1}{2.303} \frac{dN}{d\log r} = \frac{N}{\sqrt{2\pi} \ln \sigma_g} \exp \left[-0.5 \left(\frac{\ln (r/r_M)}{\ln \sigma_g} \right)^2 \right] \quad (3.13)$$

where r_M is the median radius, $\ln r_M$ is the most probable value of $\ln r$, and $\ln \sigma_g$ is the standard deviation of $\ln r$. The value $\sigma_g = 2$ corresponds to about

Table 3.1. Using various values of β , the effect of assuming the maximum radius to be 1, 10, or 100 μm is shown to be negligible on the mean radius (Davies, 1974).

β	$r_{\max} (\mu\text{m})$	$r_{\text{avg}} (\mu\text{m})$
2	1	0.18
2	10	0.20
2	100	0.20
4	1	0.13
4	10	0.13
4	100	0.13
6	1	0.12
6	10	0.12
6	100	0.12

a 100-fold radius range (Davies, 1974); larger values of σ_g would likely indicate that more than one means of particle generation is occurring and that a single log-normal distribution is not apt to fit the data well over larger radius ranges.

The log-normal distribution of Equation 3.13 fits a great deal of data and possesses unique mathematical properties (Davies, 1974) which make it easy to use. A key reason for this (Davies, 1974) is that distributions of all powers of the radius have the same value of σ_g . This is seen, e.g., in the distribution of r^3 :

$$\frac{r^3 dN}{d \ln r} = \frac{1}{2.303} \frac{r^3 dN}{d \log r} = \frac{N r_M^{1.5} r_M^{*1.5}}{\sqrt{2\pi} \ln \sigma_g} \exp \left[-0.5 \left(\frac{\ln (r/r_M^*)}{\ln \sigma_g} \right)^2 \right] \quad (3.14)$$

where r_M^* is the median radius of the distribution of r^3 . Given its applicability to aerosol size distributions, the radiative transfer model will be given a log-normal distribution as input after verifying the validity of such a distribution.

To obtain an aerosol size distribution, the first step is to calculate a mean value of $\tau(\lambda)$ for each of the four days of the experiment and fit the data to a curve of the form

$$\tau(\lambda) = b \lambda^{-\alpha} \quad (3.15)$$

where τ and λ are as defined previously, and b and α are coefficients to be determined empirically. The fit is based on the theoretically geometric association between wavelength and optical depth (Ångström, 1961).

Given the value of α for a given day, and the simple relationship (King et al., 1978):

$$v^* = \alpha + 2 \quad (3.16)$$

v^* , the Junge parameter from Equation 3.11, can be easily obtained. Using as input this calculated (not estimated) value of v^* , the wavelength-dependent optical depth values measured by the sun photometer, and the complex refractive indices for sulfate particles at wavelengths from 0.300 to 4.000 μm , the code developed by King et al. (1978) calculates a Junge distribution.

Because of the limitations encountered by King et al. (1978) and Davies (1974) in representing aerosol with a Junge distribution, a smoothing matrix is applied to the output, constraining the data to fit a log-normal distribution. From this log-normal distribution, the variables r_M and σ_g in Equation 3.14 are obtained. Table 3.2 shows that the values of r_M agree reasonably well with those of King et al. (1978). The values of σ_g are near 2.0, indicating (Davies, 1974) that a log-normal distribution is a good representation of the aerosol. The calculated v^* values are close to the assumed value (Junge, 1963) of 3.0.

Table 3.2. Calculated values of r_M , σ_g , and v^* using Mie theory.

Date	r_M (μm)	σ_g	v^*
15 Aug 1993	0.042	2.20	3.16
22 Aug 1993	0.033	2.29	3.10
23 Aug 1993	0.040	2.22	3.39
26 Aug 1993	0.032	2.25	3.35

Although the results shown in Table 3.2 seem to depict the size distribution well ($r_M \approx .04$, $\sigma_g \approx 2.0$, $v^* \approx 3.0$), there is a means of checking the code's soundness. The output of a scattering subroutine within the radiative transfer code includes extinction efficiency $Q_{ext}(\lambda)$, scattering efficiency $Q_{scat}(\lambda)$, extinction cross-section $\sigma_{ext}(\lambda)$, scattering cross-section $\sigma_{scat}(\lambda)$, and asymmetry parameter g . Optical depth $\tau(\lambda)$ is proportional to $\bar{\sigma}_{ext}(\lambda)$ through the equation (Twomey, 1977):

$$\tau(\lambda) = \int_0^z \bar{\sigma}_{ext}(\lambda) N dz \quad (3.17)$$

where N is the total number of particles per cm^3 . Since $\sigma_{ext}(\lambda)$ and $\sigma_{scat}(\lambda)$ are virtually identical in all output, it stands to reason that if $\tau(\lambda)$ and $\sigma_{scat}(\lambda)$ are plotted together (both versus wavelength), the curves should have approximately the same shape. In practice, it was necessary to multiply $\sigma_{scat}(\lambda)$ by ten to show clearly the shape of that variable (Figures 3.2-3.5) and optical depth on the same graph. It can be seen that the curves generally parallel each other, indicating that the retrieved size distribution is an adequate representation of the actual aerosol. It is also seen that the assumption of a single-scatter albedo ($\bar{\omega}_0$) equal to unity is reasonable, since σ_{ext} and σ_{scat} are nearly indistinguishable. Given the satisfactory depiction of aerosol by a log-normal distribution, such a distribution will be used in the radiative transfer model.

Optical Depth and Scattering Cross-Section Slope Comparison - August 15

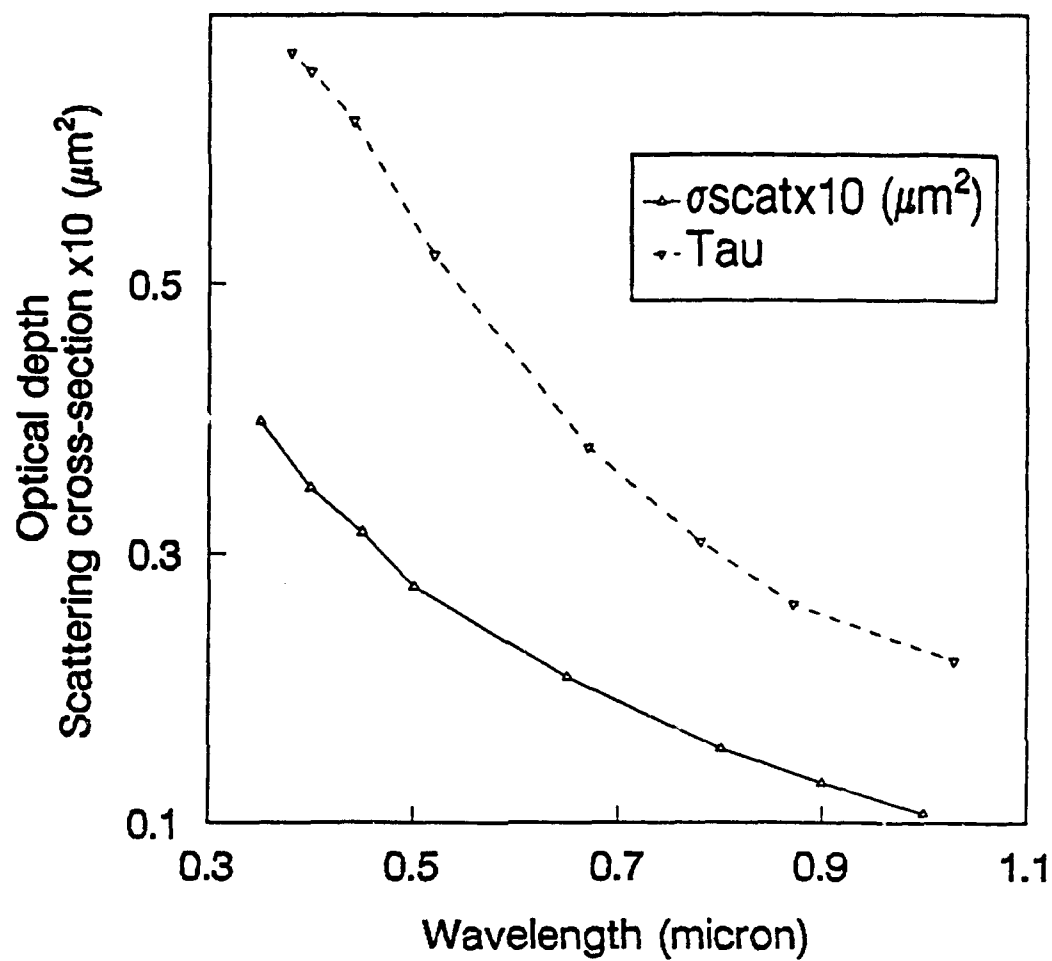


Figure 3.2. Comparison of $\tau(\lambda)$ and $\sigma_{\text{scat}}(\lambda)$ plotted versus wavelength. Data are from 15 August 1993.

Optical Depth and Scattering Cross-Section Slope Comparison - August 22

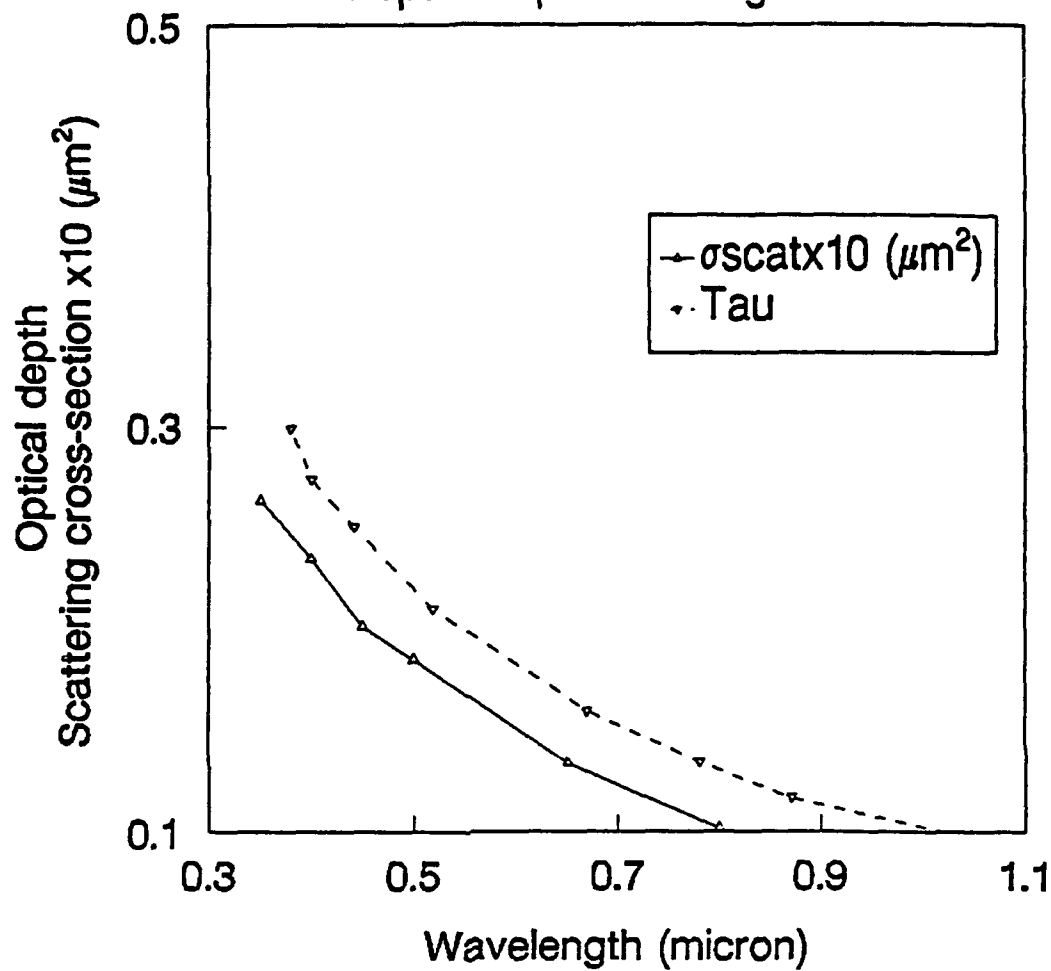


Figure 3.3. Same as Figure 3.2 except from
22 August 1993.

Optical Depth and Scattering Cross-Section Slope Comparison - August 23

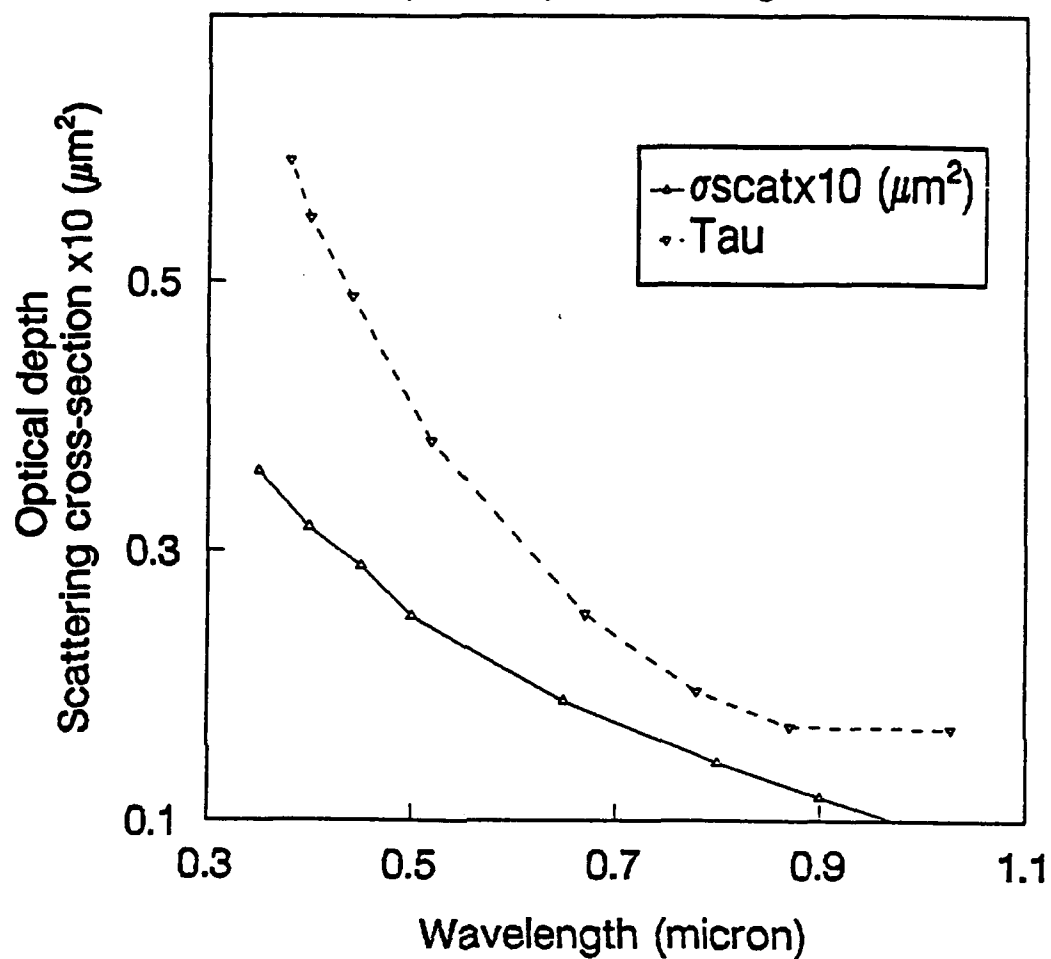


Figure 3.4. Same as Figure 3.2 except from 23 August 1993.

Optical Depth and Scattering Cross-Section
Slope Comparison - August 26

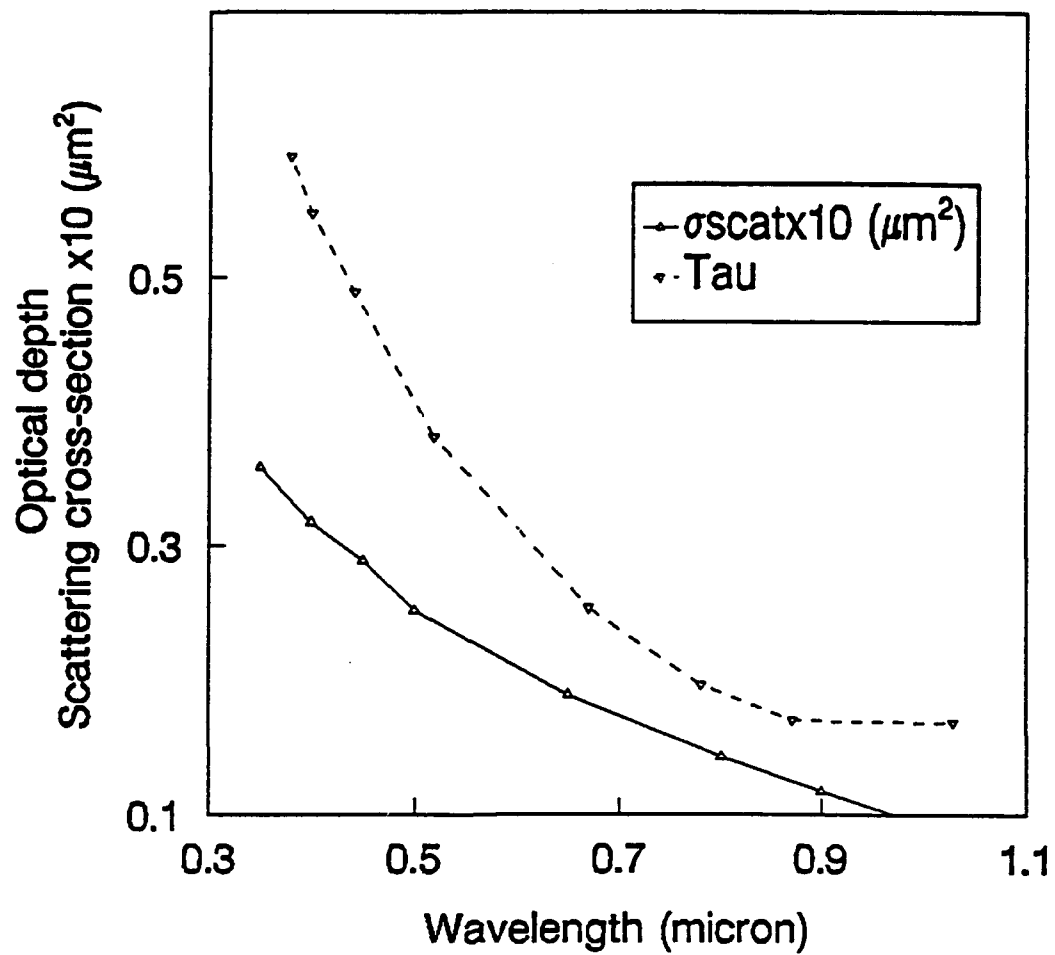


Figure 3.5. Same as Figure 3.2 except from
26 August 1993.

3.5. Model Description and Verification.

With all preliminary calculations performed, the model can now be run to determine its validity, adjusted if necessary and then used to learn the impact of sulfate haze on the surface radiation budget. At this point it will be helpful to review the algorithm and the assumptions made therein.

This model employs a tridiagonal matrix (Toon et al., 1989) based on the two-stream formulation used by Meador and Weaver (1980). It arose from a need for a routine which could calculate the radiation fields in a plane parallel, vertically inhomogeneous, multiple scattering atmosphere without undue computational demands. Though many have developed numerically efficient, approximate radiative transfer schemes, this model was developed to deal with three seldom-addressed problems: allowance for a vertically inhomogeneous atmosphere, calculation of photolysis rates in anisotropic, multiple-scattering atmospheres, and treatment of scattering in the presence of thermal emission.

A single homogeneous layer is the simplest way to represent the entire atmosphere; several approximate techniques (Toon et al., 1989) have been developed to compute the transfer of solar energy through such a layer. These procedures are all referred to in the literature as "two-stream" approximations; each individual method is identified by a specific name such as the quadrature or δ -Eddington technique.

Beginning from the solution for the intensity at the boundaries of a single homogeneous vertical layer, Shettle and Weinman (1970) found that a matrix of equations could be derived for the intensities at the boundaries of multiple inhomogeneous layers by matching the single-layer equations using appropriate boundary conditions. Lacis and Hansen (1974) showed that when solar forcing was treated as a boundary condition, the single-layer, two-stream solutions for reflectivity and transmissivity could be placed into an adding and doubling form for multiple layers, resulting in a tridiagonal matrix. The benefit of this form of matrix (Toon et al., 1989) is that the equations can be solved without resorting to a complex matrix inversion, and the computational time increases only linearly with increases in the number of vertical levels. Hansen et al. (1983) showed how the equations could be extended for a quadrature form of the two-stream approximation when the solar zenith angle is included explicitly.

Toon et al. (1989) derived a tridiagonal matrix for multiple layers valid for the entire class of two-stream equations (Meador and Weaver, 1980); the matrix is the backbone of this model. First, the general two-stream solution for a single homogeneous layer is derived. Next, a matrix solution for multiple homogeneous layers, which approximates a vertically inhomogeneous atmosphere, is derived. The next step is to introduce the two-stream source function approximation, and then the accuracy of the technique is demonstrated using specific examples. The advantages provided by this scheme are that it retains the speed, simplicity, and numerical stability of the Lacis and Hansen (1974) approach, without being

restricted to a single type (e.g., quadrature or δ -Eddington) of two-stream approximation. A drawback of this approach (Toon et al., 1989) is that while its accuracy for multiple layers is usually better than ten percent for heating rates, the model's error can approach twenty percent when the solar zenith angle is large. For this experiment, however, that shortcoming is irrelevant since measurements were always taken between 0900 and 1600 local time due to difficulties in aligning the sun photometer at other times. The radiative transfer model is thorough and versatile in its representation of the atmosphere, and is reliable enough to be used to determine aerosol effects on surface shortwave flux.

This model is capable of handling as many as 55 vertical layers; input here include the 33 layers generated by the water vapor model and the user-defined boundary layer height. The algorithm integrates over 26 different solar wavelength intervals to get the total flux. Since the sun photometer data consist of optical depth at eight wavelengths, none of which corresponds to those in the model, it was necessary to develop a means of taking the photometer data and transforming them into the form required by the model. The wavelengths ranged from 0.380 μm to 1.029 μm in the case of the sun photometer, and from 0.256 μm to 4.292 μm in the model, meaning that both interpolation and extrapolation were necessary. Though extrapolation was seemingly a risky venture, it is useful to recall that a curve fit can be done using Equation 3.15. Instead of using a mean value of optical depth over a given day, however, this time a curve is fit

to each ten-minute average of optical depth. The result is an excellent fit to data points (Figure 3.6); the close correspondence between data and the geometric curve allows the user to transform the eight sun photometer points into the twenty-six points necessary for model input with minimal uncertainty.

The radiative transfer model requires several parameters to calculate shortwave surface flux; these include Q_{ext} , Q_{scat} , g , r_M , σ_g , $q(z)$, and $\tau(\lambda, z)$. Of these, all but $\tau(\lambda, z)$ need to be calculated by intermediate algorithms prior to running the radiative transfer model. In the case of $\tau(\lambda, z)$, the values of optical depth are known at the surface from sun photometer data, and are transformed from eight values to twenty-six using the curve fit described by Equation 3.15. However, the measured data only reveals $\tau(\lambda)$ at the surface ($z=0$). Aside from determining how to extrapolate values of optical depth, it was also necessary to apportion the aerosol optical depth as a function of height. This was accomplished by taking the aerosol optical depth (as a function of wavelength) and dividing by the estimated boundary layer height. With this number calculated, the optical depth is computed as a simple linear function of height within the boundary layer. That is, the optical depth decreases linearly from its maximum (measured) surface value to zero at the top of the boundary layer. Above the boundary layer, the aerosol optical depth is assumed to be zero. The altitudes at which $\tau(\lambda, z)$ is calculated are the 33 levels generated by the water vapor distribution model plus the user-defined top of the boundary layer; $\tau(\lambda, z)$ thus consists of optical depth at 26 wavelengths and at 34 levels.

Geometric Curve Fit 15 August/0827 EST

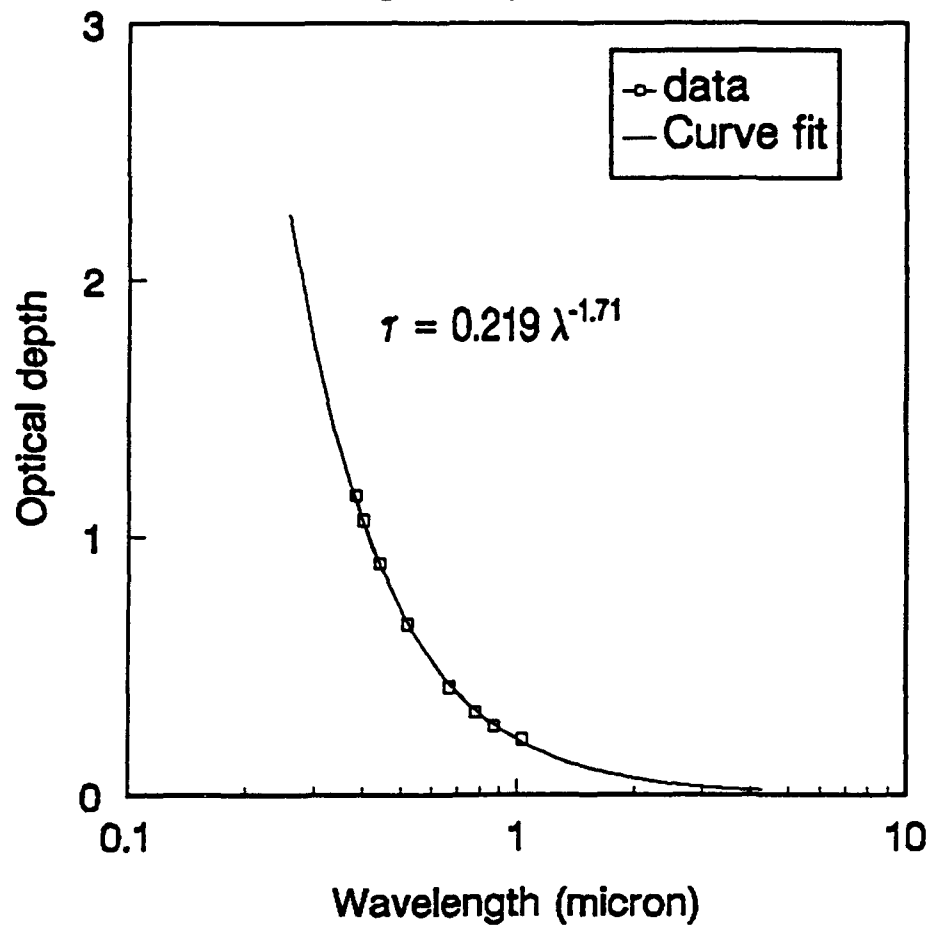


Figure 3.6. A comparison of the sun photometer data points and the curve following the equation $\tau = 0.219(\lambda^{-1.71})$. Data shown are from 15 August 1993 at 0827 EST.

Gases of particular importance in this model are water vapor, carbon dioxide, and ozone, because of their important absorption and scattering properties. The model calculates the component of optical depth due to gases based on absorption and scattering which results from the presence of just the three gases above. The vertical profiles of these trace gases are taken from a U.S. Standard Atmosphere mid-latitude sounding. Attenuation in this program is divided into four categories: trace gas absorption; aerosol absorption; molecular (Rayleigh) scattering; and absorption and scattering by clouds.

Since the incident angle of sunlight is so important, this model calculates ephemeris data which requires only the input of the day, month, and year by the user; input files with optical depth data must associate a time with the $\tau(\lambda, z)$ to allow the model to compute the zenith angle. The optical depth model input was $\tau(\lambda, z)$ for 26 wavelengths and 34 levels in the model; the values of optical depth were obtained using the curve fit and linear interpolation methods already described. The ten-minute averaging period was chosen to keep the number of data points reasonable without allowing the zenith angle to vary excessively.

As discussed in Section 3.4, one value of the parameters r_M , σ_g , and v^* was computed per day. While the variables r_M , σ_g , and v^* are as important as optical depth input, the former were considered less variable than the latter, which is why the averaging periods are significantly different. The variables r_M , σ_g , and $\tau(\lambda)$ are necessary input for the radiative transfer model to calculate Q_{ext} , Q_{scat} , ω_0 , and g , which are in turn needed to calculate shortwave surface flux.

Given the input of solar variables, water vapor distribution, aerosol size distribution, a model atmosphere, and vertical layers, the program computes fluxes using a tridiagonal matrix. The model was first tested by providing aerosol optical depth input and comparing the flux output with measured values. Before making decisions about the accuracy of the model, however, there were two final steps to take: first, determine the inherent error of the pyranometer, and second, allow for a bias between model output and measurements which arises because of their different spectra. The combination of cosine and temperature effects under the experimental conditions gives a maximum error of two percent (manufacturer specifications), or about 10-15 W/m² for typical measured values. The offset between the data sets involved more thought: since the pyranometer measures flux between 0.295 and 2.800 μm , and the code takes into account wavelengths between 0.256 and 4.292 μm , the model output should by that fact alone always be slightly larger. Though the discrepancy is small, it should be calculated as accurately as possible to estimate its effect on the results and its significance compared with the pyranometer error. To determine the difference, it was necessary to integrate Planck's law (Wallace and Hobbs, 1977) in its exact form:

$$E_{\lambda} = \frac{c_1 \lambda^{-5}}{\exp(c_2/\lambda T) - 1} \quad (3.18)$$

where E_{λ} is the monochromatic flux, c_1 has a value of $3.74 \times 10^{-16} \text{ Wm}^2$, c_2 is

equal to $1.44 \times 10^3 \text{ m}^\circ\text{K}$, λ is a given wavelength, and T in this case is equal to 6100°K , the temperature of the sun.

To estimate the amount by which the flux is reduced when ignoring the "tails" of the solar emission curve, Equation 3.16 was integrated (actually approximated using finite differencing) twice - once with the upper and lower limits set at 0.295 and $2.800 \mu\text{m}$, and then with the limits at 0.256 and $4.292 \mu\text{m}$. In each case the finite difference $d\lambda$ was set at $0.001 \mu\text{m}$. When dividing the second answer by the first, the ratio was 1.025 , indicating that the pyranometer would yield answers about 2.5 percent lower than those given by the model, even assuming both are perfect. For this reason, when plotting the calculated fluxes versus the measured ones (Figure 3.7), the line $y = 1.025x$ was included as the baseline indicating perfect agreement (note that a 2.5 percent error amounts to $10\text{-}20 \text{ W/m}^2$ for the range of fluxes measured in this experiment).

Though Figure 3.7 shows reasonable agreement between calculated and measured fluxes, there are points from August 15 and August 26 that lie well off the expected line. When the data analysis was started, even the most marginal data were kept. Good and bad data were initially differentiated by examining flux curves as a function of time; if the curves varied smoothly, the data were deemed acceptable. One problem with this is that there were few good data, and slight departures from a smooth curve were ignored in the interest of maximizing the data set. In the case of the measurements that remain, ten-minute averages were taken during good data periods, with marginal information

Calculated vs. Measured Flux

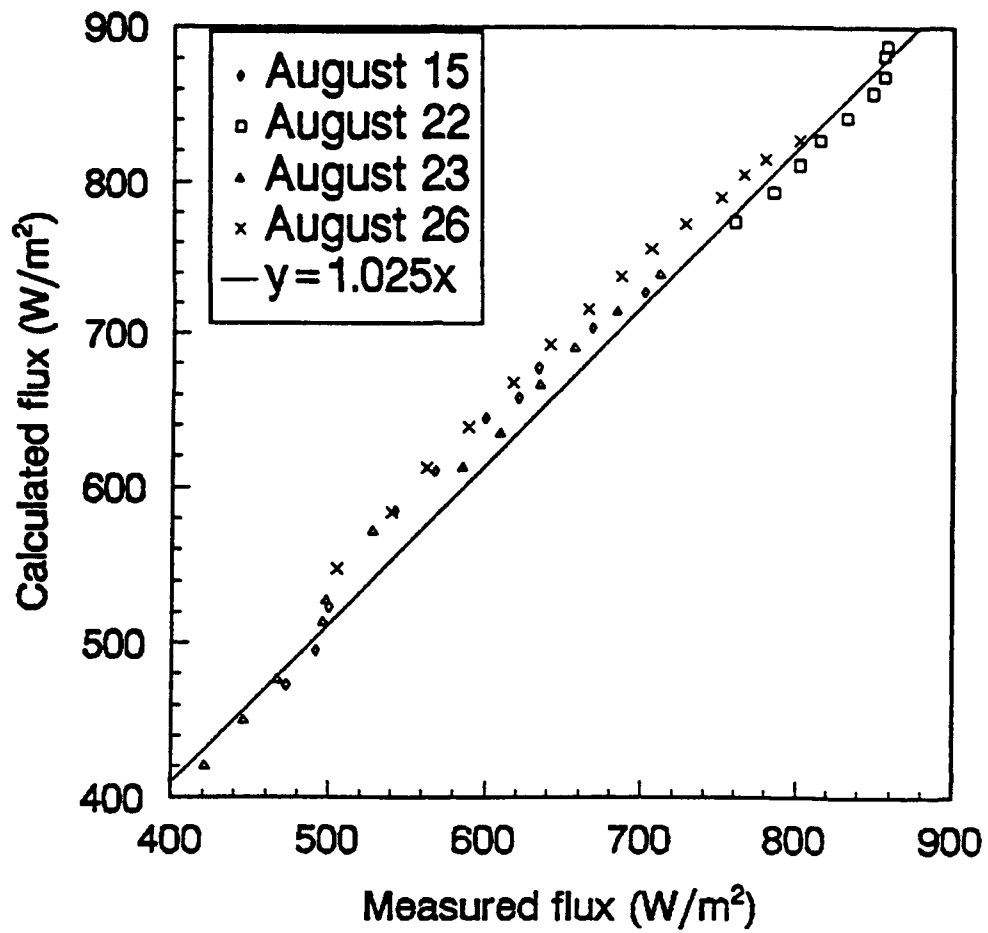


Figure 3.7. A scatter plot of calculated vs. measured fluxes. The line $y = 1.025x$ is the expected result given the use of a slightly larger spectrum by the model than by the pyranometer.

sometimes remaining near the beginning or end of the period. A journal kept during the research is annotated with remarks indicating stratocumulus and cumulus over the mountain ridge during parts of good data periods. Clouds not directly in the sun photometer's view do not affect the optical depth data, but even clouds on the horizon may adversely affect the readings of the 180-degree FOV pyranometer used to measure surface fluxes. If points affected by any cloud cover, as determined by journal annotations and inspection of solar flux curves, are deleted (which amounts to rejecting the last third of the August 15 data and the last half of the August 26 data), much better agreement exists (Figure 3.8) between calculated and measured fluxes. In every case of large discrepancy in Figure 3.7, the measured flux is smaller, bolstering the notion that clouds reduced the amount of radiation striking the sensor. Figure 3.9 is a plot of observed surface flux versus time on August 26. The vertical lines delimit the bounds of good data, yet it can be seen that the surface flux does not follow a smooth curve for the latter part of the period in question, probably indicating the presence of scattered clouds (journal entries past 1600 UTC confirm cumulus clouds on the horizon). When data are restricted based on a combination of the surface flux curve and the journal entries, the model verifies well.

As a further check of the model's validity, the fractional error in the data from Figure 3.8 is calculated; this fractional error f is defined as

$$f = (F_{\text{obs}} - F_{\text{calc}})/F_{\text{obs}} \quad (3.19)$$

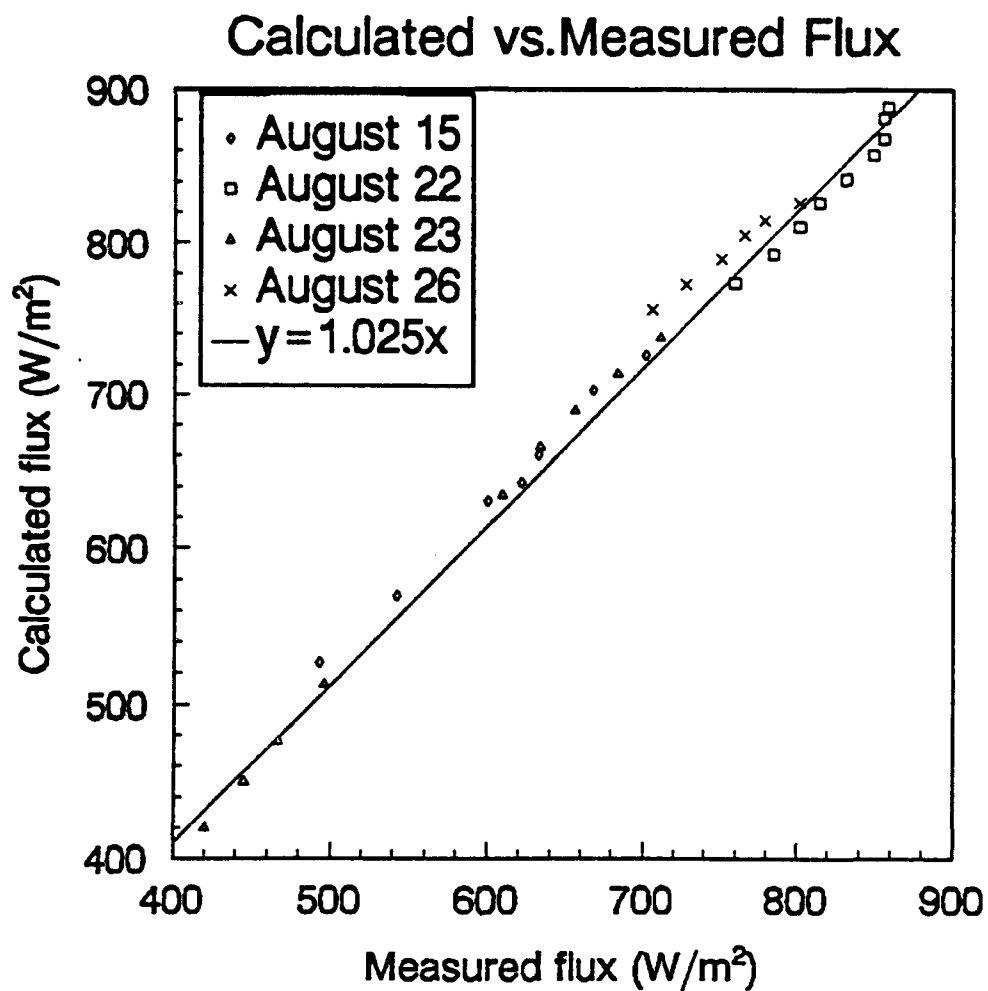


Figure 3.8. Same as in Figure 3.7, but with marginal data from August 15 and 26 deleted.

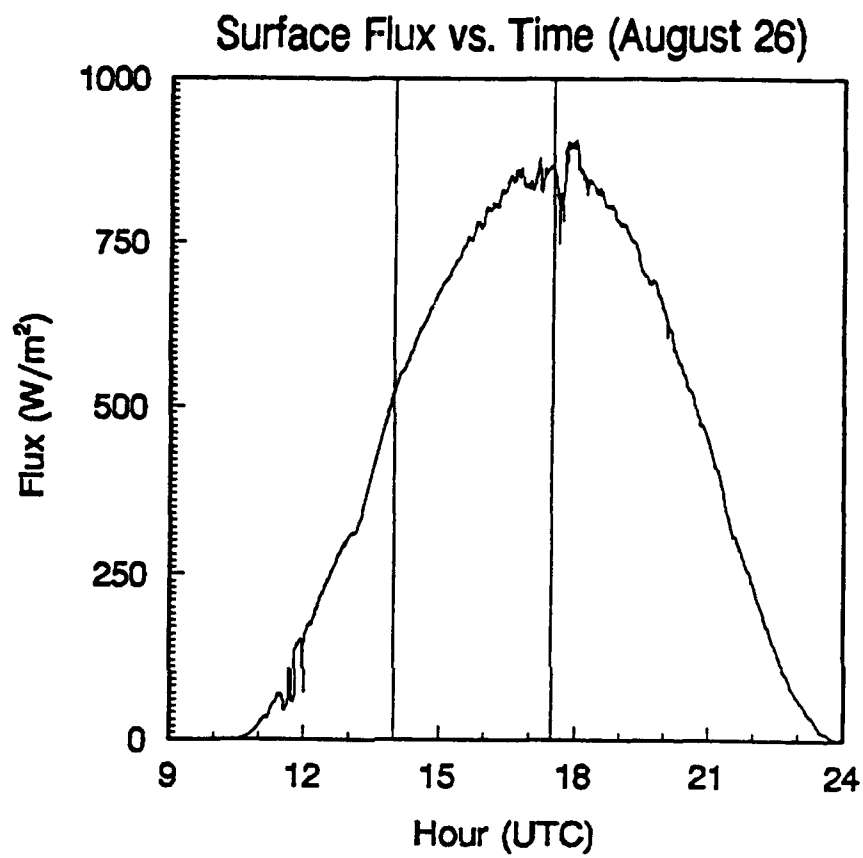


Figure 3.9. Surface flux vs. time plot from August 26.

where F designates flux, the subscripts distinguish between observed and calculated fluxes, and where all calculated fluxes have been reduced by 2.5% to account for the different wavelength ranges of the model and the pyranometer. The fractional error is then plotted in histogram form (Figure 3.10) to determine its distribution and thus the extent of agreement between calculated and measured fluxes. The sample interval is set at 0.005. Figure 3.10 shows peaks at ± 0.02 , and reveals that virtually all points are inside the ± 0.03 range, an indication of excellent agreement. Finally, the mean and standard deviation of f are calculated and found to be -0.0064 and 0.0216, respectively, showing that the fractional error is centered near zero as well as tightly confined to values near the origin. All evidence supports the conclusion that the model agrees well with measurements, and use of the code to explore haze effects is justified.

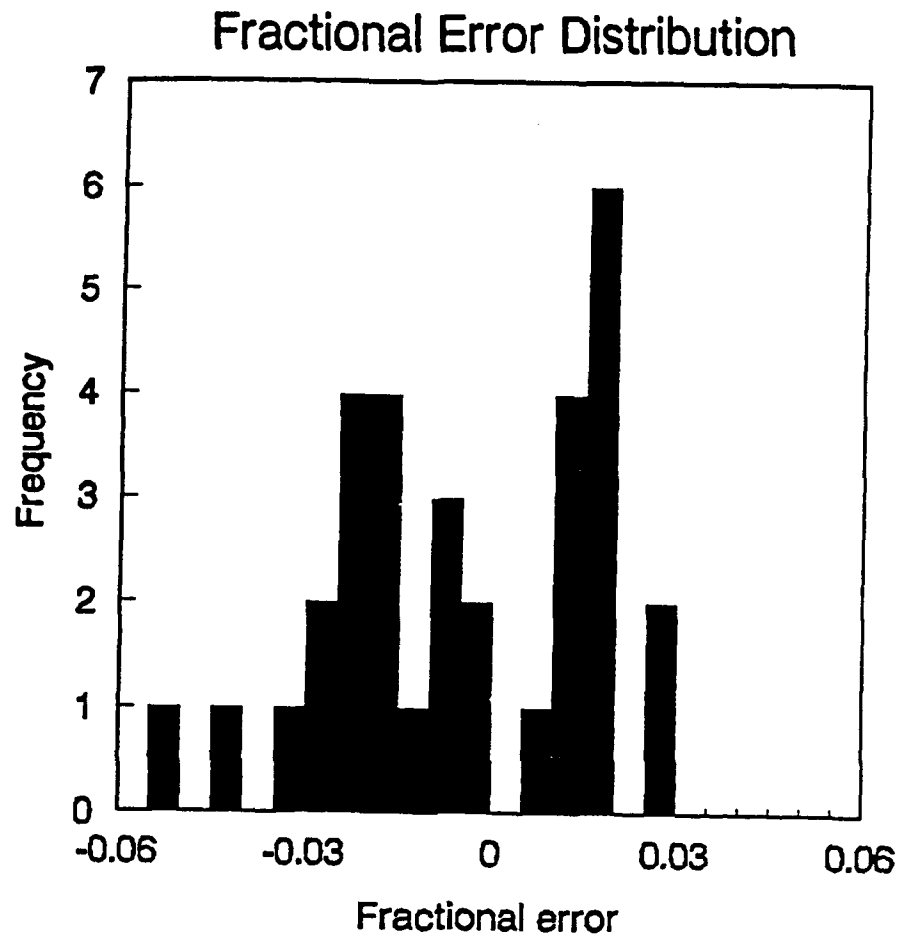


Figure 3.10. A histogram of fractional error distribution indicates that nearly all points have errors of less than three percent.

Chapter 4

COMPARISON OF INSOLATION WITH AND WITHOUT AEROSOL PRESENT

The verification of the model in Chapter 3 is an important step toward assessing the role aerosol plays in determining the surface radiation budget, but it is still only an intermediate process. The next step is to try to determine the effect of aerosol optical depth and varying zenith angle on the surface radiation budget, and ascertain whether or not the attenuation of radiation can be related to commonly-measured meteorological parameters. If a strong relationship is found, climate modelers could use the information to parameterize sulfate haze. Given the wealth of research into the growth of particles as a function of relative humidity (Ångström, 1961; Davies, 1974; Leaitch et al., 1986, O'Neill et al., 1993), the effects of relative humidity on visibility (Ball and Robinson, 1982; Fitzgerald et al., 1982), and the frequency with which these variables are measured, it seems logical to examine aerosol attenuation of radiation as a function of relative humidity and visibility.

Evaluation of aerosol effects on visibility turned out to be a practical impossibility for a variety of reasons. The first plan was to measure the scattering coefficient with a nephelometer, but the instrument lacked the required accuracy. An alternative was to measure the boundary layer height dz

with a laser beam ceilometer and use the relationship $\tau = (k_{\text{ext}})(dz)$ to infer the extinction coefficient, which closely approximates the scattering coefficient in the case of sulfate aerosol (Blanchet, 1989). This strategy also fell short because the ceilometer was not precise enough for this experiment. Finally, our last resort was to estimate the boundary layer height using radiosonde data; the sondes were launched once a day. Since the estimate of dz is subject to a great deal of uncertainty to begin with, and is calculated only once a day, its use in determining scattering coefficients for data averaged every ten minutes would be pointless. The conclusion is regrettable but inescapable: this experiment will yield no new information about the relationship between aerosol optical depth and visibility.

Measurements of relative humidity, unlike those of visibility, were reliable. They were averaged every ten minutes along with optical depth data, allowing a fairly straightforward comparison of net flux reduction and humidity at the surface. Before beginning the analysis, prudence dictated a classification of data into separate categories based on the day on which they were obtained. The reason for this is simple: though all data were taken deliberately during similar weather (i.e., hazy, cloud-free), they were nevertheless measured on four different days during an eleven-day period between 15 and 26 August 1993. Given that the air mass was at least slightly modified from one day to the next, any relationships that might be valid on one day are not necessarily true at another time.

A good starting point in examining the role of aerosol on the surface radiation budget is to plot aerosol optical depth at 519 nm as a function of time. The wavelength was chosen because it is the closest of the sun photometer's channels to the maximum solar output computed (Wallace and Hobbs, 1977) by Wien's Law. Such a graph (Figure 4.1) allows for inspection of columnar aerosol changes on a given day, and also permits a comparison of varying air quality on different days. Data from all four days show considerable fluctuations in optical depth values; also of note is the fact that the air seems to be significantly cleaner on August 22 and August 26 than on the other two days measurements were taken. Optical depths on all days generally trend toward a minimum at solar noon, because the values are of vertical optical depth. The period of nearly constant optical depth on August 26 beginning at about 10:00 EST will provide an opportunity to examine the cosine effect on flux losses; since τ_{aer} is unvarying, changes in μ_0 may dominate flux changes during that interval.

Another worthwhile step is to explore the progression of relative humidity as a function of time (on a day-by-day basis). Relative humidity is vitally important to this study; particle sizes are known to increase with increasing relative humidity (Hänel, 1976). It is being evaluated for a possible correlation to surface flux losses; such a relationship might facilitate parameterization of sulfate haze by climate modelers. In addition, plotting humidity allows an examination of the way in which the meteorological situation evolved on a given day. Figure 4.2 illustrates two important points. Not surprisingly, relative

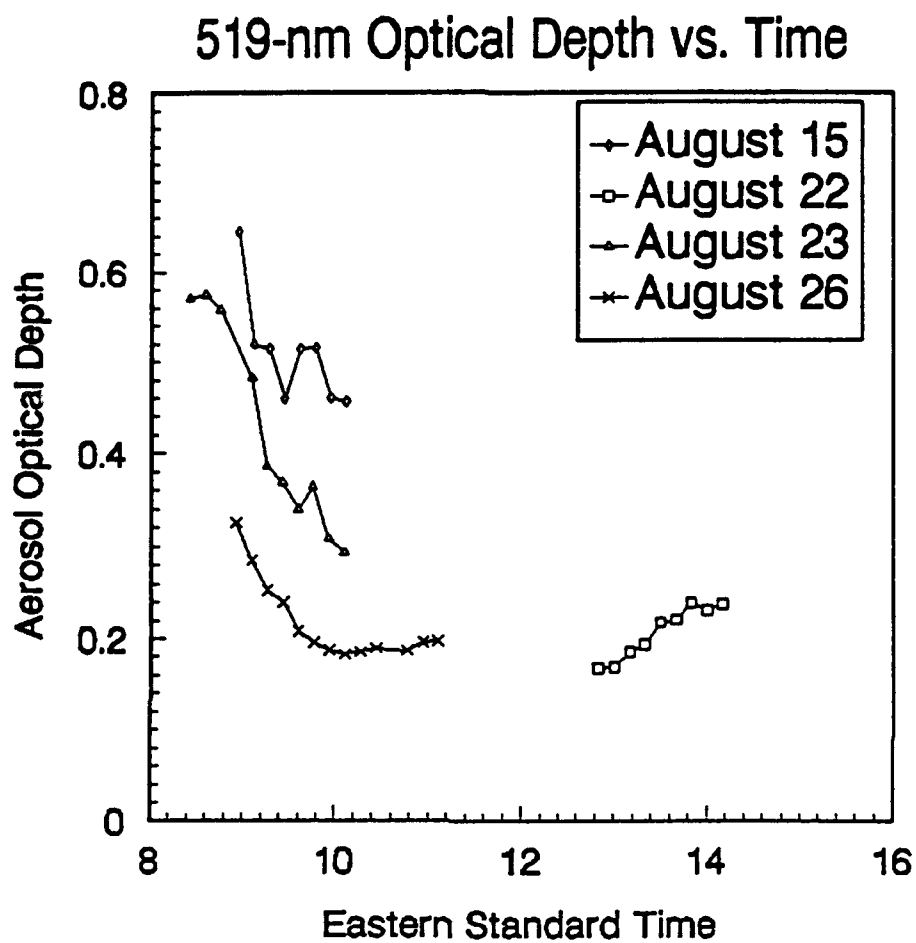


Figure 4.1. The optical depth at 519 nm is shown for all days of the experiment.

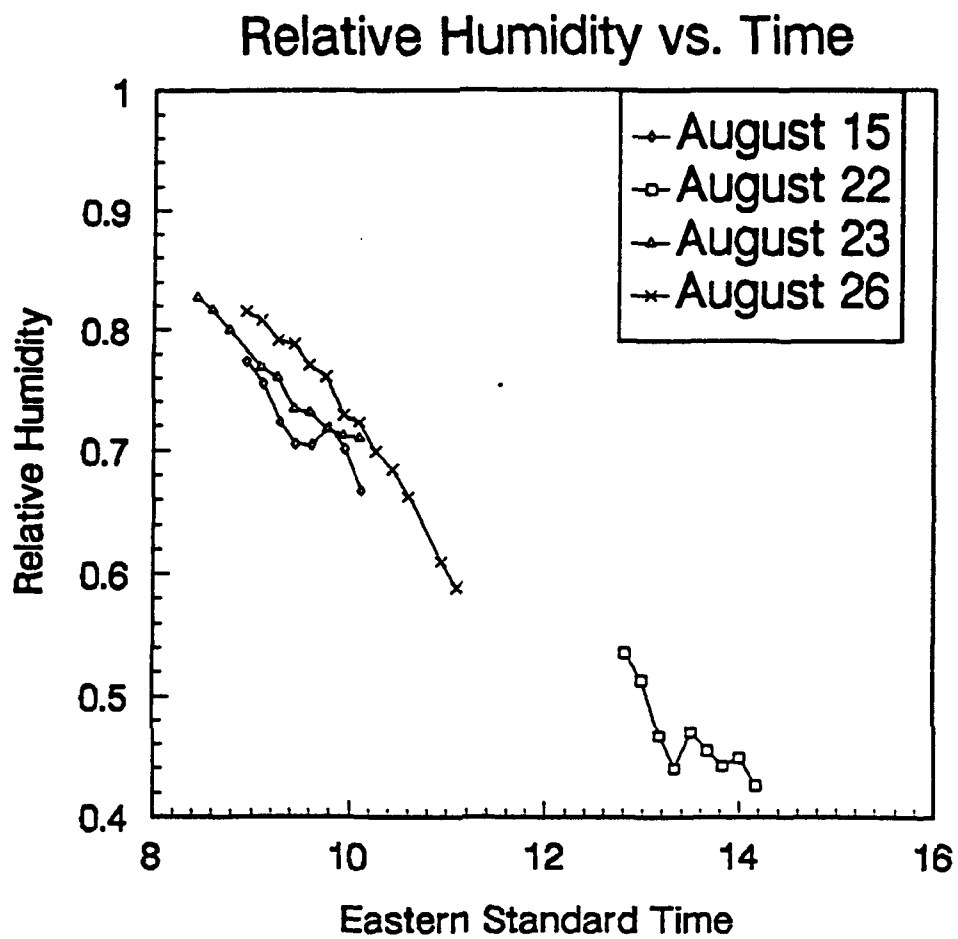


Figure 4.2. Relative humidity is plotted as a function of time.

humidity shows a downward trend from morning to afternoon as air temperature rises. Also, its values on August 22 are much lower than on any other day of the experiment, possibly explaining that day's apparent higher air quality.

To learn the effects of aerosol on midlatitude summer insolation, the surface fluxes with and without aerosol present, and the differences between the two, are plotted. It should be noted that the surface flux with aerosol present is the calculated, not measured flux. The reason is that when flux changes are calculated, the results are a small deviation between two large numbers. If measured fluxes, with their random instrument error of 10-20 W/m² and imperfect accord with model output, were used to calculate the difference, each individual deviation would be subject to large uncertainty.

The observed solar flux in August is about (Figures 4.3-4.6) a maximum of 900 W/m². Surface flux is a fairly smooth function of time in these cases because of the absence of cloud cover, but not perfectly so because of variations in optical depth. The flux computed by the model with no aerosol input is absolutely smooth, since the model need only take into account solar output, Earth-Sun geometry, molecular absorption by H₂O, CO₂, and O₃, and Rayleigh scattering. Without aerosol, the maximum calculated surface insolation nears 1000 W/m². Inspection of these curves thus indicates that aerosol accounts for attenuation on the order of 100 W/m² during hazy summer days in the northeastern United States. Losses of that magnitude are definitely significant to climate.

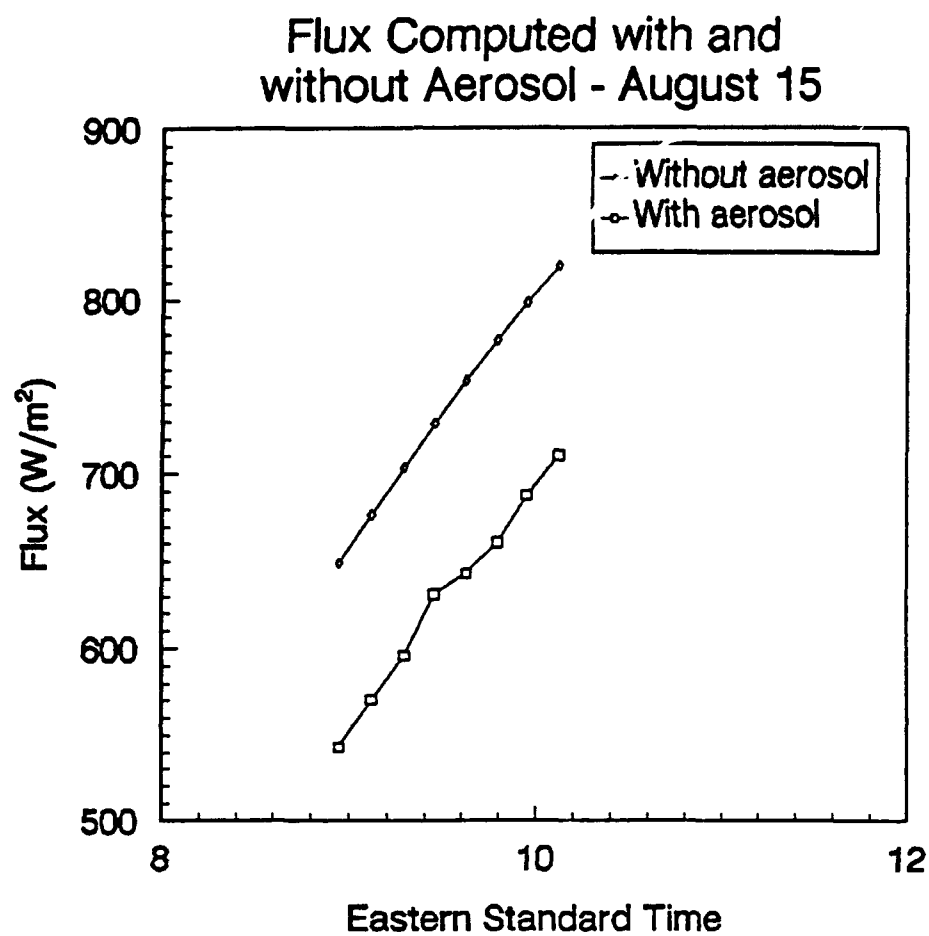


Figure 4.3. Surface flux computed with and without aerosol present is shown for August 15.

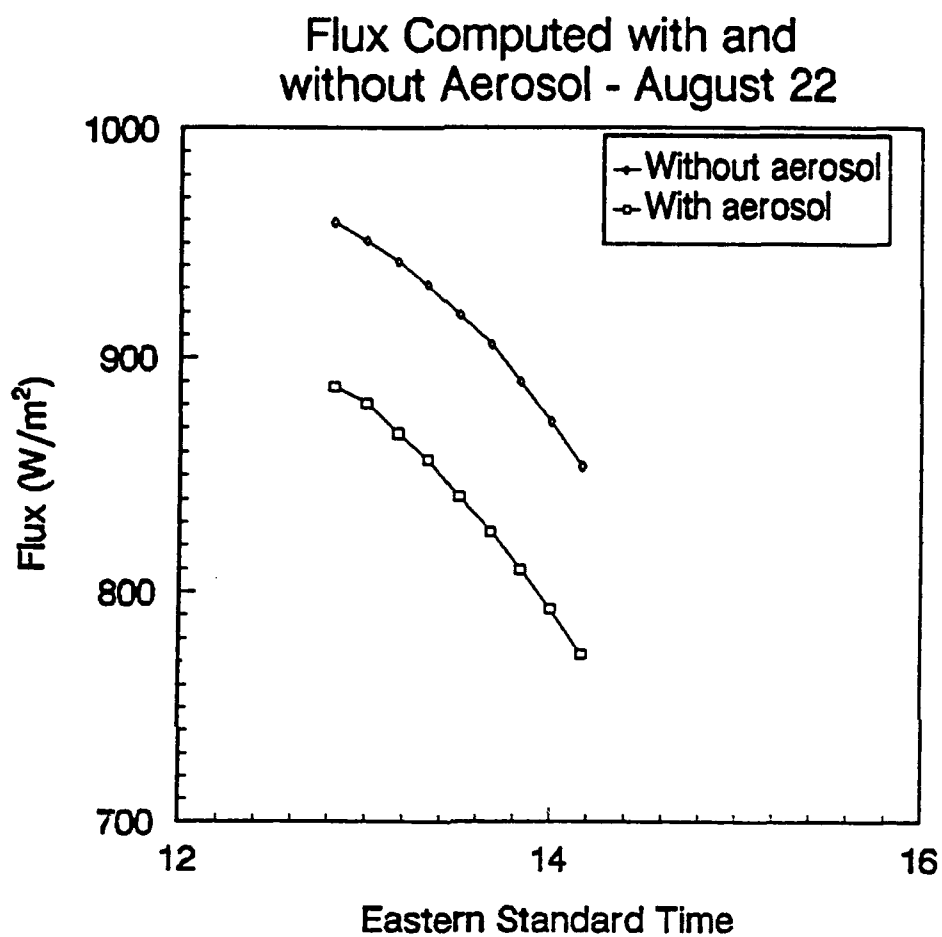


Figure 4.4. Same as Figure 4.3, but for August 22.

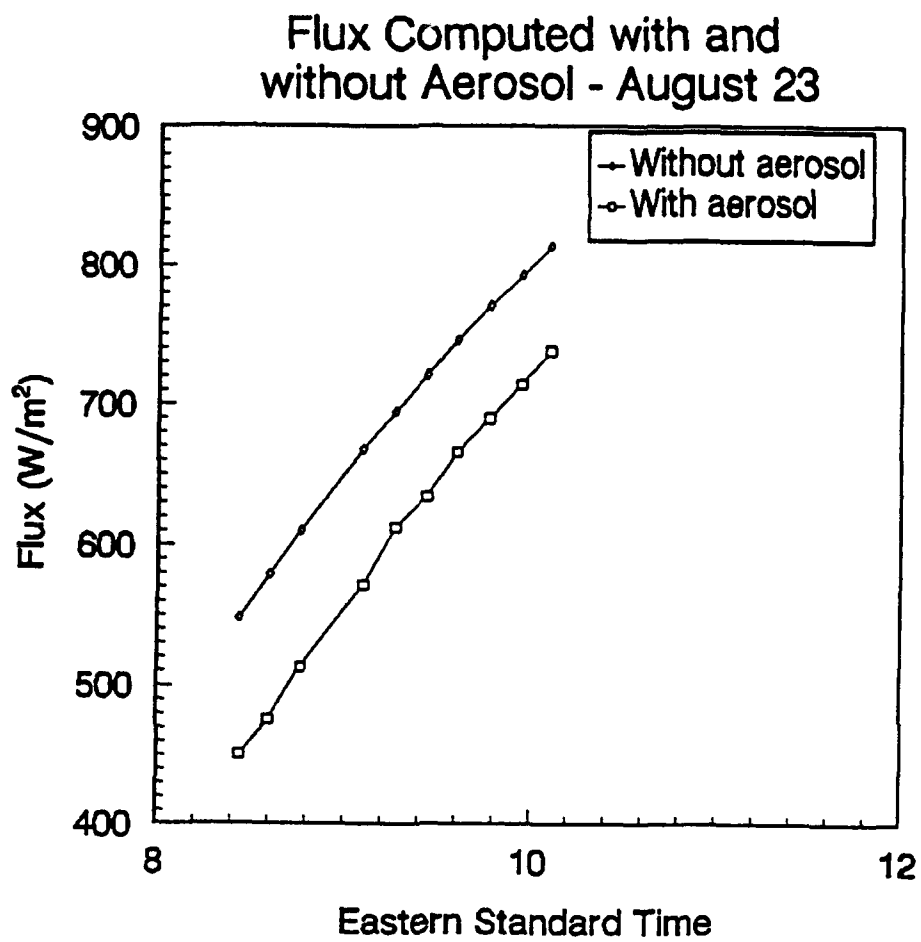


Figure 4.5. Same as Figure 4.3, but for August 23.

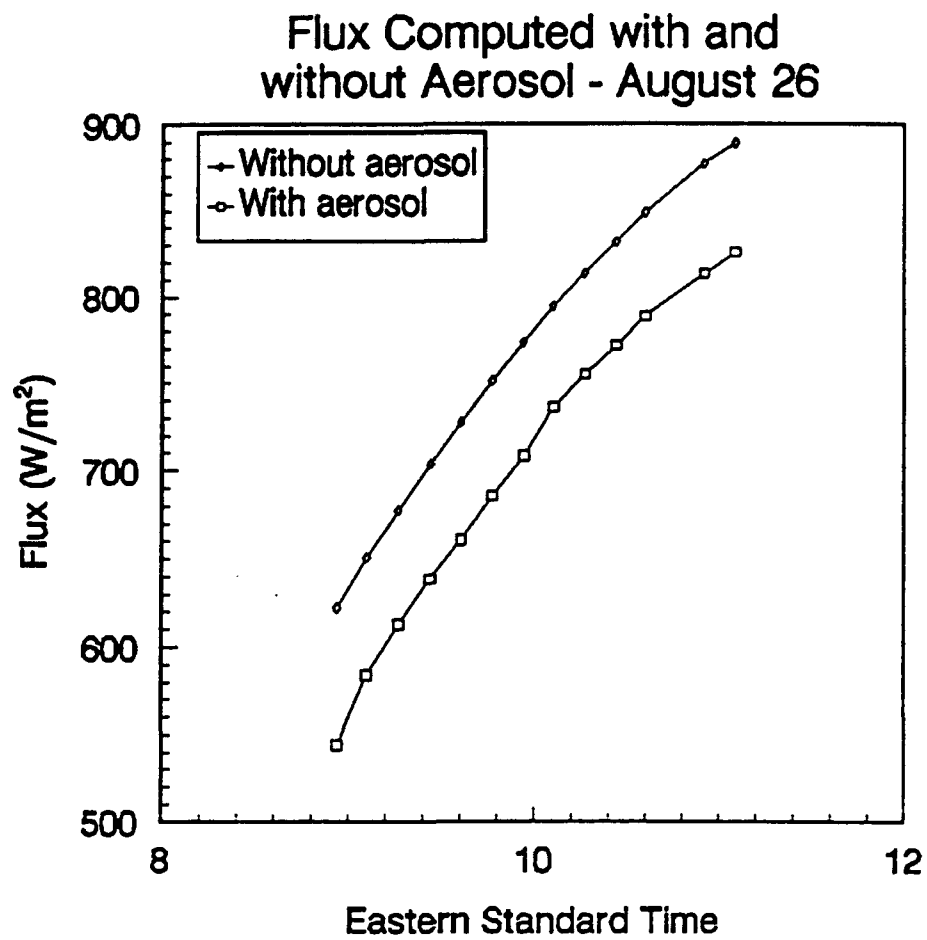


Figure 4.6. Same as Figure 4.3, but for August 26.

The net flux change ΔF , defined as $F_{\text{clr}} - F_{\text{aer}}$ with the subscripts denoting clear skies (no aerosol; Rayleigh scattering only) and the presence of aerosol, respectively, is plotted as a function of time. Figure 4.7 illustrates several important points. To a first approximation, the curves in Figure 4.7 resemble those in Figure 4.1, indicating the expected relationship between aerosol optical depth and attenuation. Also, the decrease appears to change uniformly with time only on August 22; the absolute reduction on three of the four curves tends toward a minimum at noon, despite the opposite trend in insolation. Finally, during the August 26 period of near-constant optical depth beginning around 10:00 EST, the flux loss is almost constant but increases slightly. The total shortwave transmission T is defined (Goody, 1964) as:

$$T = F_{\text{aer}}/F_0 \quad (4.1)$$

where F_{aer} is the downward shortwave flux at the surface and F_0 is the downward shortwave flux at the top of the atmosphere. The total shortwave transmission T can be expressed as the sum of the direct and diffuse beam components

$$T = T_{\text{dir}} + T_{\text{diff}} \quad (4.2)$$

The two components are defined as:

$$T_{\text{dir}} = \exp(-\tau/\mu_0) \quad (4.3)$$

where τ is total optical depth and μ_0 is the cosine of the zenith angle, and

$$T_{\text{diff}} = (\pi F \mu_0)^{-1} I(\tau) \quad (4.4)$$

where πF is the incident collimated flux per unit area perpendicular to the earth's surface (using the plane parallel atmosphere approximation) and $I(\tau)$ is

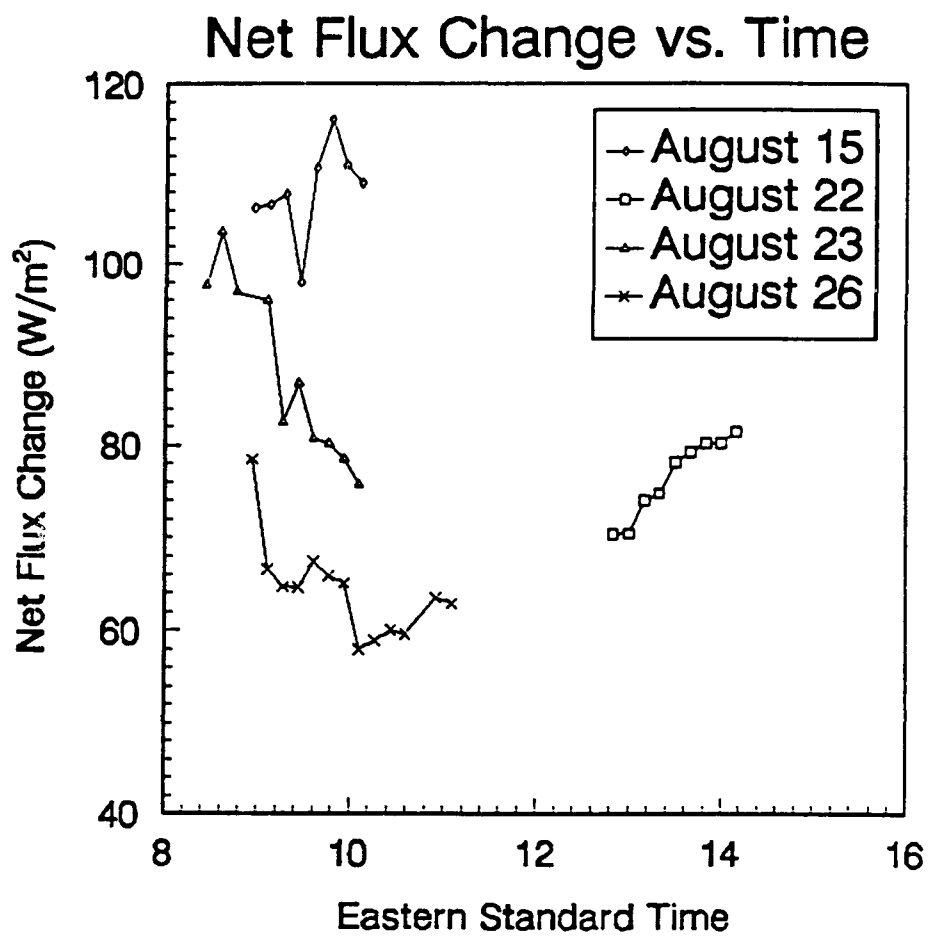


Figure 4.7. Net flux change due to aerosol as a function of time.

the downward diffuse flux. If there were no aerosol in the atmosphere, Equation 4.1 could be written

$$T_{clr} = F_{clr}/F_o \quad (4.5)$$

where F_{clr} would be the downward shortwave flux calculated at the surface without aerosol, and T_{clr} would be the transmission in the absence of aerosol. By combining Equations 4.1 and 4.5, it is seen that F_{aer}/F_{clr} , the ratio of downward shortwave surface flux with aerosol present to that of downward shortwave surface flux with aerosol absent, can be expressed as T/T_{clr} . By using Equations 4.2-4.4, T/T_{clr} can be rewritten as

$$T/T_{clr} = [\exp(-\tau/\mu_o) + (\pi F \mu_o)^{-1} I(\tau)]/T_{clr} \quad (4.6)$$

The net flux change ΔF is defined as $F_{clr} - F_{aer}$, so the ratio F_{aer}/F_{clr} is equal to $1 - \Delta F/F_{clr}$. Since F_{aer}/F_{clr} is equivalent to T/T_{clr} , Equation 4.6 can be rewritten:

$$\Delta F/F_{clr} = 1 - [\exp(-\tau/\mu_o) + (\pi F \mu_o)^{-1} I(\tau)]/T_{clr} \quad (4.7)$$

If optical depth is constant and μ_o nearly so, Equations 4.3 and 4.7 imply that direct transmission is nearly constant and depends strongly on μ_o . Equations 4.3 and 4.7 refer to broadband optical depth, but 519-nm optical depth varies with broadband optical depth. Therefore, since the direct component is a sizable portion of total transmission, it is expected that net flux loss at around 10:00 EST on August 26 should be approximately constant, which Figure 4.7 shows is the case. The slight increase in ΔF during the period beginning at around 10:00 EST is attributable to the slow increase in μ_o occurring at that time.

There was a large range of flux values ($400\text{--}900\text{ W/m}^2$) resulting from widely varying values of μ_o computed in this experiment. Since this range could by itself influence the value of ΔF , it was decided to calculate and plot the quantity $\Delta F/F_{dr}$. The point was to remove the μ_o dependence to first order by dividing by the incident flux, which itself is a function of μ_o . Removing the μ_o dependence would determine whether flux losses near noon were a result of the larger initial fluxes. Figure 4.8, which depicts the fractional flux losses $\Delta F/F_{dr}$ as a function of time, shows an even greater correlation with Figure 4.1 than does Figure 4.7. The quantity $\Delta F/F_{dr}$ is plotted to allow inspection of flux losses at any given time on a more objective basis. Like the net flux loss in Figure 4.7, the fractional flux loss during the minutes shortly after 10:00 on August 26 is approximately constant.

Given the reasonable similarity among the Figures 4.1, 4.7, and 4.8, it seems likely that flux loss plotted against optical depth would show a relationship as well. Net flux loss (Figure 4.9) is clearly seen to be a function of optical depth except on August 15, when such a connection is not obvious. Total transmission depends on both direct and diffuse beams. Flux loss should therefore be a strong function of optical depth. However, flux loss will not have the perfect exponential relationship with optical depth shown in Equation 4.3, because diffuse transmission increases (Wallace and Hobbs, 1977) with optical depth, and because of the dependence of net flux loss on μ_o .

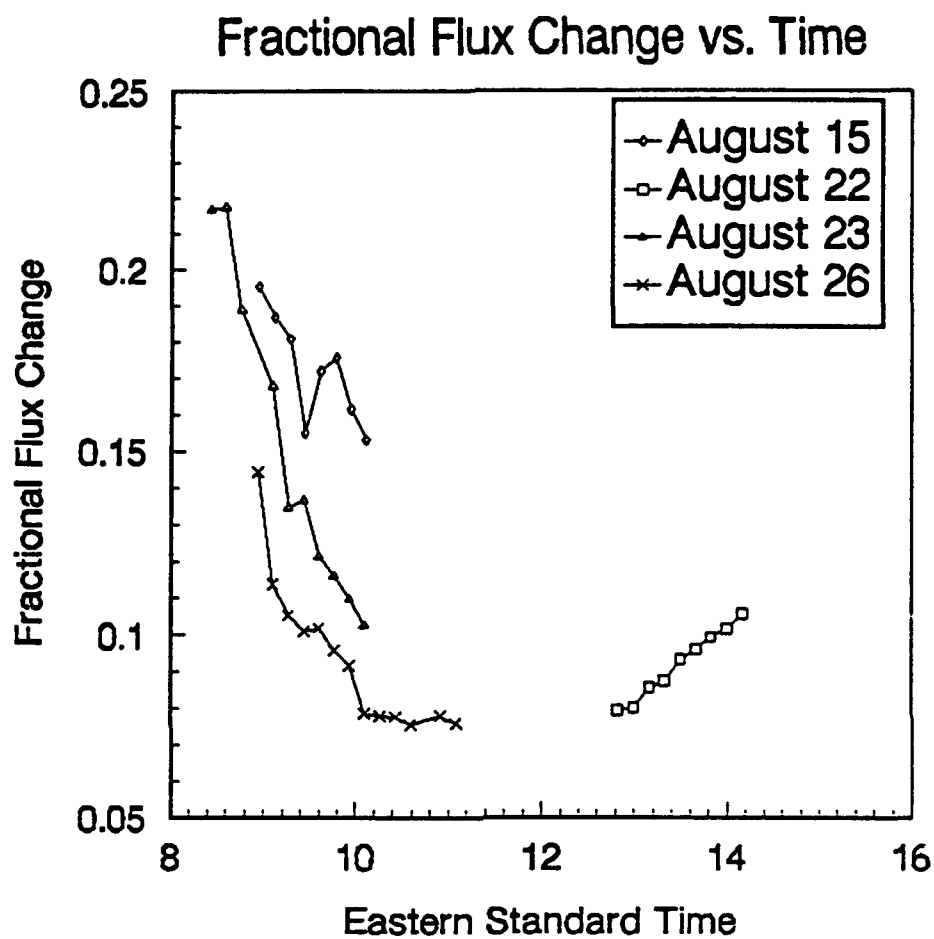


Figure 4.8. Fractional flux change due to aerosol as a function of time.

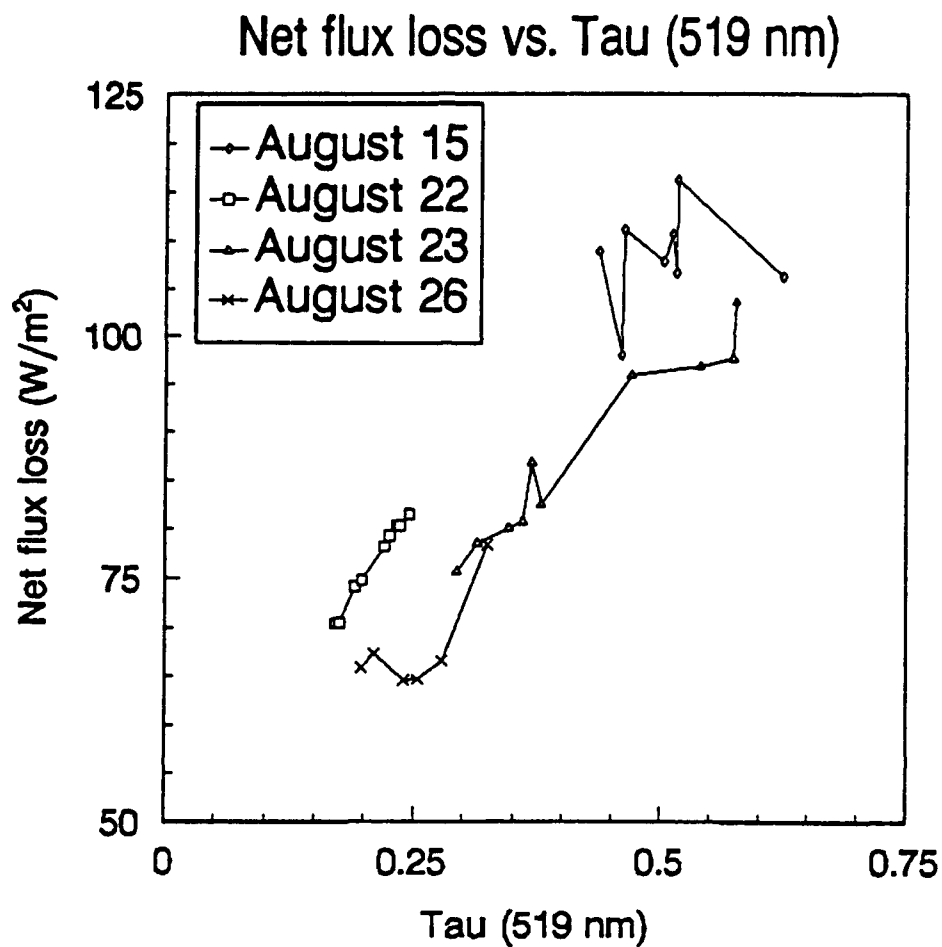


Figure 4.9. Net flux loss is plotted against optical depth.

When fractional flux loss is shown (Figure 4.10) as a function of optical depth, the expected strong correlation emerges. As with net flux loss, data from August 15 show the least agreement between measurements and theory; values from the other three days are seen to increase nearly monotonically with optical depth. The data also show, importantly for climate modelers, that aerosol extinction alone can in hazy conditions exceed twenty percent. Additional information can be gained by taking all points on Figure 4.10 and fitting a curve to them. Since the points from all days appear to fall approximately on one line, a linear regression is chosen. When a linear regression is performed, the best-fit curve is

$$\Delta F/F_{\text{clr}} = 0.293\tau + 0.028 \quad (4.8)$$

where τ is the 519-nm aerosol optical depth. The correlation coefficient of the curve is 0.97. Figure 4.11 illustrates the excellent fit of Equation 4.8, as was expected given the high correlation coefficient.

The linearity of $\Delta F/F$ when plotted as a function of optical depth is intriguing. It is known from Equation 4.7 that, at least to a first approximation, $\Delta F/F_{\text{clr}}$ is an exponential function of optical depth. A possible reason for the linearity is that $e^{-\tau}$, for small optical depth values, can be approximated using a Taylor expansion as:

$$e^{-\tau} = 1 - \tau + \tau^2/2! - \tau^3/3! + \dots + \tau^n/n! \quad (4.9)$$

Clearly, for very small optical depth values, only the first two terms on the right would be significant, and $\Delta F/F$ as a function of optical depth would be nearly

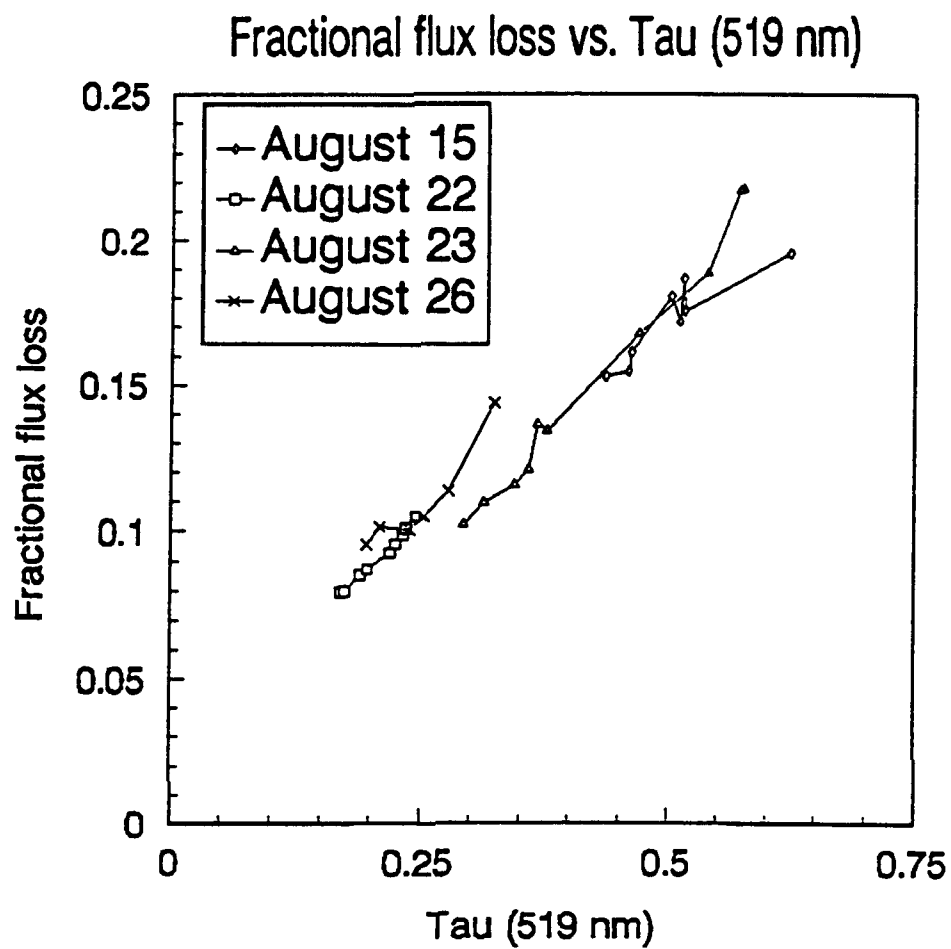


Figure 4.10. Fractional flux loss is shown as a function of optical depth.

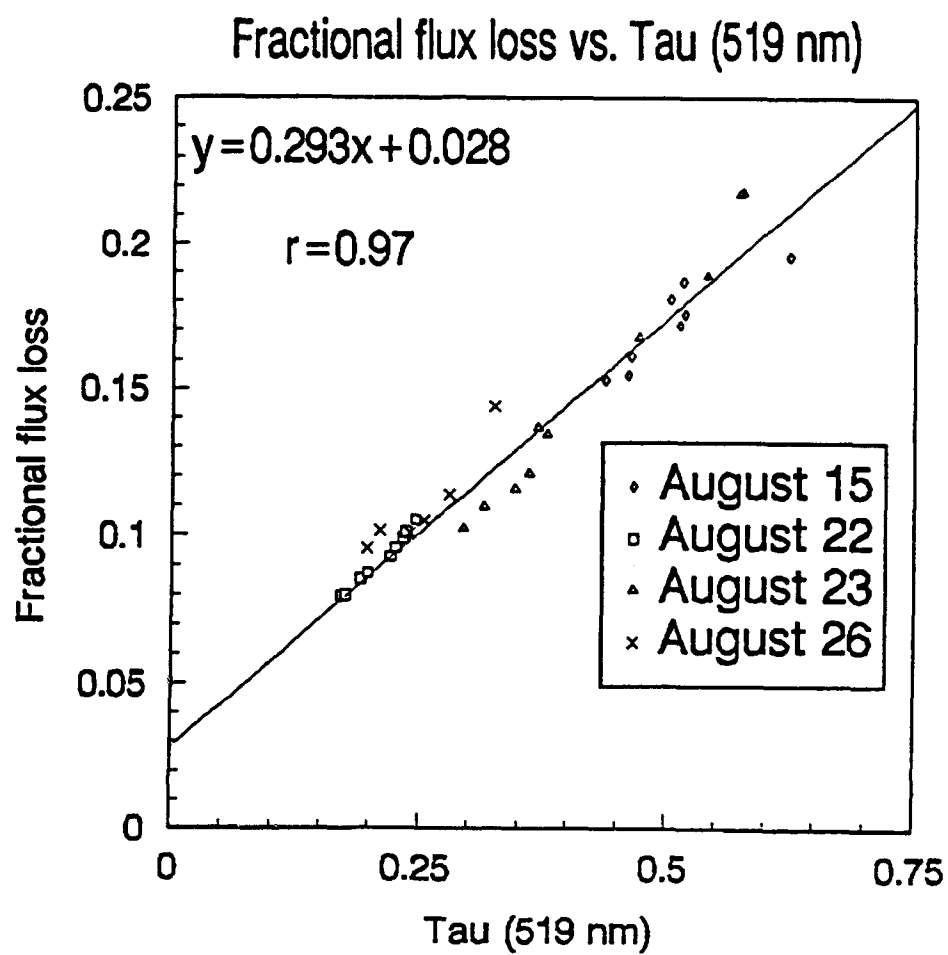


Figure 4.11. Data points from Figure 4.10 are shown with a best-fit curve.

linear (disregarding μ_0 and diffuse transmission). The smallest values of optical depth measured in this experiment were between 0.15 and 0.25; at those values only the linear term of the Taylor expansion would need to be considered. For higher values of optical depth, which in this study are between 0.6 and 0.7, $e^{-\tau}$ would deviate considerably from linearity.

Equation 4.8, though a superior fit to measurements, presents a problem for climate modelers in that the y-intercept is nonzero due to measurement error. Based on Equation 4.8, there is a fractional flux loss of nearly three percent due to aerosol when the aerosol optical depth is zero! While modelers find it necessary to make physical assumptions and approximations, it is certainly of no advantage to them to insert obviously false statements into their algorithms.

Since Equation 4.8 would require modelers to use an incorrect assumption in their code, the data from Figure 4.10 were again fitted to a line, but this time with the intercept forced to zero. In this case, the result is

$$\Delta F/F_{\text{clr}} = 0.363\tau \quad (4.9)$$

Equation 4.9 still has a high correlation coefficient of 0.94; the line is shown in Figure 4.12.

Equation 4.9 could prove very beneficial to climate modelers. It states that if the 519-nm optical depth is known (from Chapter 2, continuous optical depth measurements may in the future be inexpensive to obtain with a rotating shadowband radiometer), the fractional flux loss due to aerosol can be easily calculated. In fact, there would be no need to measure fluxes directly; if

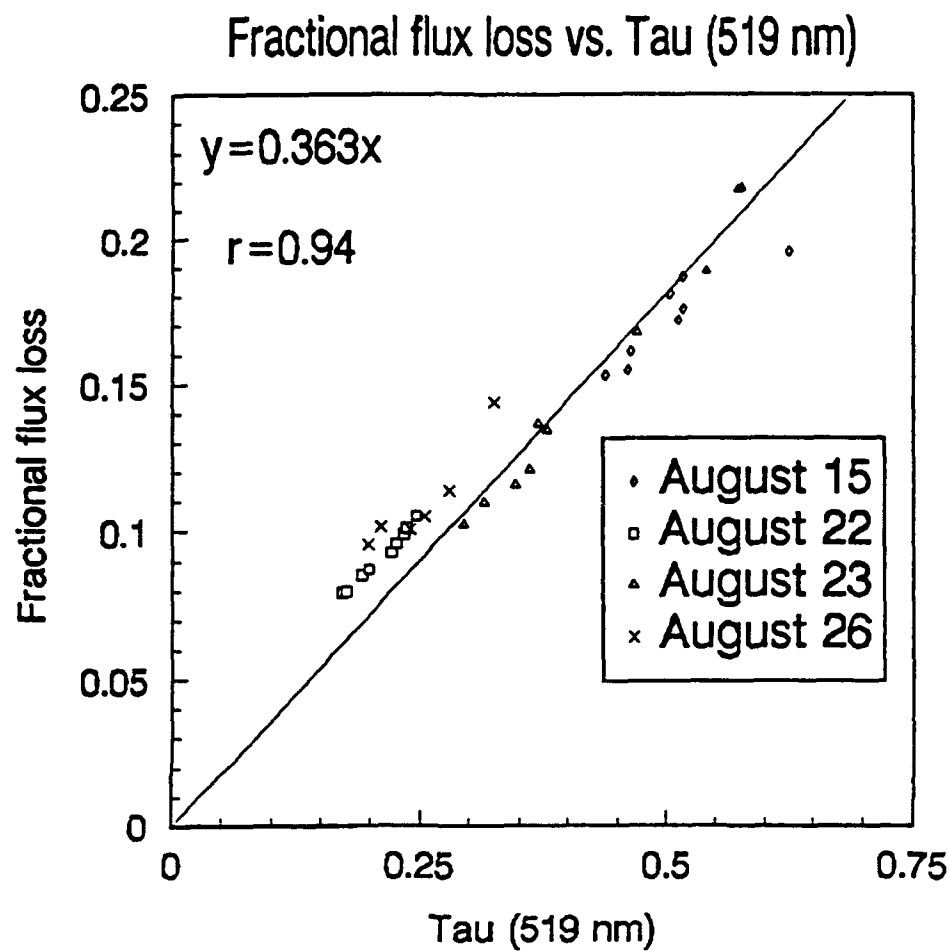


Figure 4.12. Same as Figure 4.11, but with y-intercept forced to zero.

modelers are only interested in the fractional flux depletion as a function of optical depth, Equation 4.9 allows the ratio to be found with no measurements aside from optical depth itself.

The Rock Springs experiment was designed to measure the magnitude of aerosol attenuation, and it has shown that flux reductions of ten to twenty percent are not uncommon during the summer months in the industrialized northeastern United States. Another useful discovery is the relationship found between fractional flux loss and optical depth in Equations 4.8 and 4.9. With the initial goal thus accomplished, the second aim is to determine if flux attenuation can be parameterized as a function of relative humidity. Optical depth was plotted (Figure 4.13) against relative humidity (on a given day) to examine the possibility of finding an empirical relationship. If one could be found, there would be an implication of a similar connection between loss and relative humidity. Figure 4.13 shows interesting results: on all days but August 22, a strong relationship exists between 519-nm optical depth and relative humidity. On August 26, when surface relative humidity values were the highest during this study, the dependence of optical depth on relative humidity is unmistakable. On August 22, it could easily be argued that optical depth is completely independent of relative humidity; measurements were taken during the afternoon with low surface relative humidities and the correlation is expected to be smaller than on the other days.

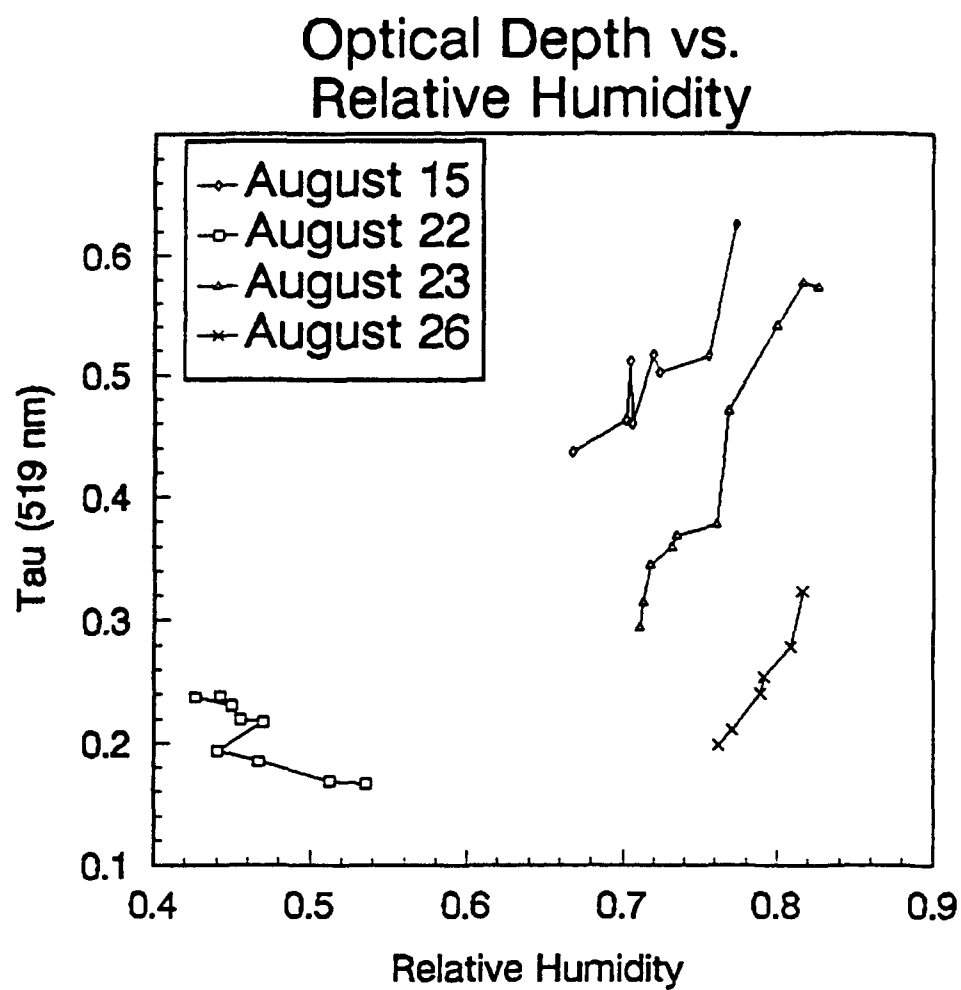


Figure 4.13. Optical depth is shown plotted against relative humidity.

There are a couple of possible reasons that no connection was found on August 22: first, it is possible that sulfate aerosol is generally unresponsive to changes in relative humidity below 70-80%. In studies by Fitzgerald et al. (1982) and Hänel and Zankl (1979), any empirical rules are stated by the authors to show better results at relative humidities exceeding 85% than at lower values. It is notable that in this experiment, the surface humidity is always less than 83%; on August 22, the value never exceeds 55%. On August 23 and August 26, when the surface relative humidity is greater than 80%, the relative humidity values aloft will likely approach saturation within the boundary layer, and will certainly be higher than at the surface. On those days, a strong correlation is expected and found between net flux loss and surface relative humidity. Though Fitzgerald et al. (1982) and Hänel and Zankl (1979) each showed that droplet size could be linked to relative humidity, their growth functions showed only slight positive slopes at humidities between 30% and 80%. The idea that the growth of sulfate particles is only weakly tied to relative humidity on August 22 is worth consideration.

Another plausible reason for the weak link between optical depth and surface relative humidity on August 22 was suggested by O'Neill et al. (1993) after their experiments showed a slight negative correlation between net flux loss and relative humidity. Their theory was that in a well-mixed boundary layer, as was present during the Rock Springs research, convection decreases surface relative humidity while increasing its value at higher levels (i.e., water vapor as

well as sensible and latent heat is redistributed by convection). The convection would then slightly increase the optical depth above the surface, and the change in optical depth from the ground to the top of the layer would be changed in an uncertain fashion. With limited radiosonde launches, changes in aerosol size distribution as a function of height are impossible to know, but the theory of O'Neill et al. (1993) is credible, as is the first possibility that sulfate aerosol does not respond strongly to increases in relative humidity at values less than 70-80%. It is also important to note that data from August 22 were the only ones taken in the afternoon. At that time there would definitely be a well-mixed boundary layer; that is assumed in the morning as well but perhaps incorrectly. Either or both theories could be correct; what is definitely known is that optical depths measured on August 22 seem unrelated to relative humidity.

Since optical depth and attenuation are closely linked, and optical depth is sometimes a function of relative humidity, there should be a correlation between flux losses and relative humidity and thus a possibility of parameterizing sulfate haze. To examine this prospect requires an investigation of net flux loss as a function of relative humidity. Figure 4.14 shows a fairly strong relationship between the two on August 23 and August 26, but not on the other two days. On August 15, flux losses are highly variable, just as they were when plotted against optical depth. On August 22, the lack of correlation, as with optical depth, probably stems from low relative humidity values.

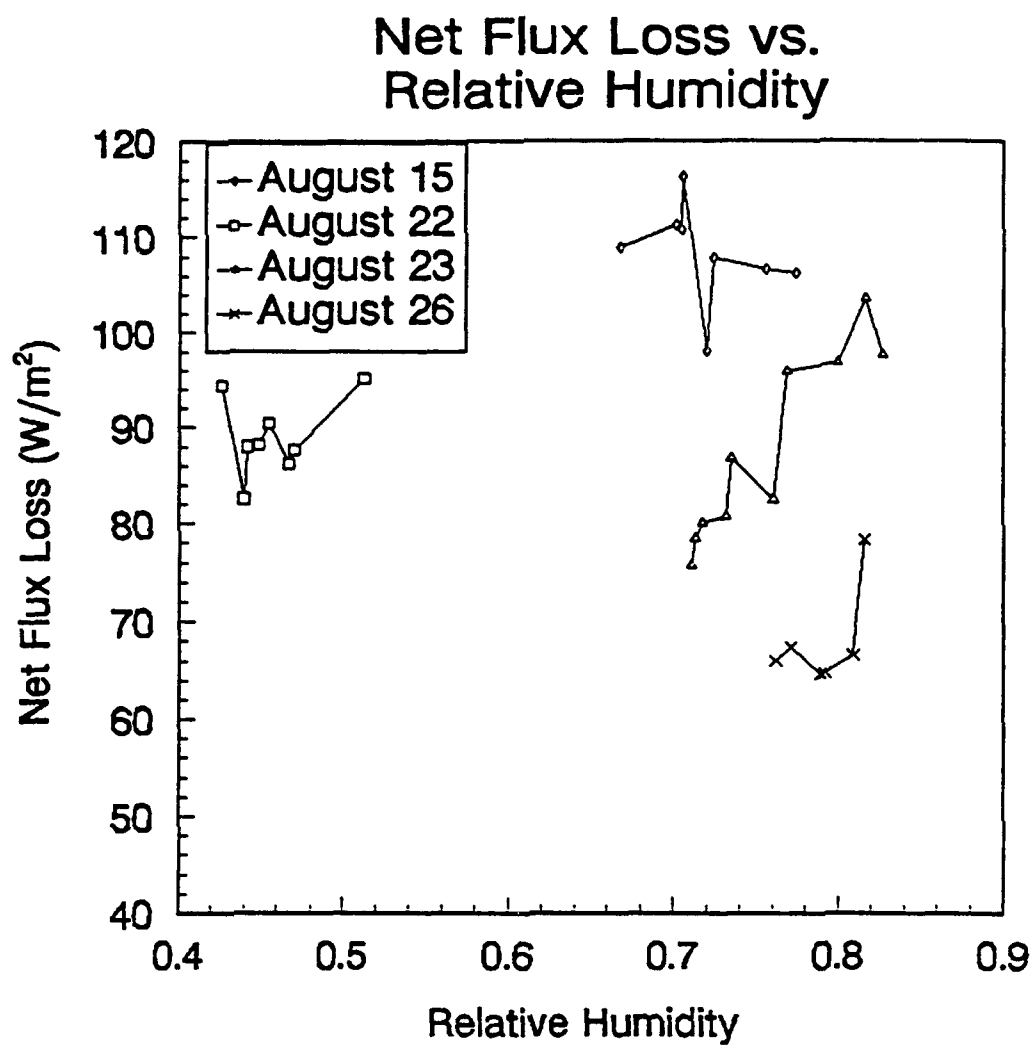


Figure 4.14. Net flux loss is shown as a function of relative humidity.

Fractional flux loss as a function of relative humidity (Figure 4.15) is seen to be a function of relative humidity on all days but August 22. It appears that when the cosine dependence is removed from consideration, the August 15 data, though still a bit irregular, generally can be considered a function of relative humidity. Fractional flux losses on August 23 and 26 are even more strongly related to relative humidity than are net flux losses, and the slopes of three of the days are very similar, even though they do not merge as neatly as did the curves of fractional flux reduction versus optical depth. The similar shapes are likely due to the relative humidity dependence; the reason for not merging into one line is probably a result of the optical depth dependence. An idea for future research would be to normalize data like those in Figure 4.15 to a "dry optical depth", that is, take all optical depth values and divide by an optical depth taken on the same day at, for example, 50% relative humidity. The idea is similar to dividing flux losses by insolation to eliminate the μ_0 dependence; it was impossible to implement here due to lack of data. If normalization were done, the roughly parallel curves in Figure 4.15 might merge into one line as do the curves in Figure 4.10.

The Rock Springs experiment, based on the results in this chapter, has answered questions about the effects of aerosol and the likelihood that these effects can be parameterized. In the former case, a general statement is that aerosol reduces surface flux by 10-20% on hazy summer days in an industrial area of this country. As for relating that effect to meteorological variables, it

Fractional Flux Loss vs. Relative Humidity

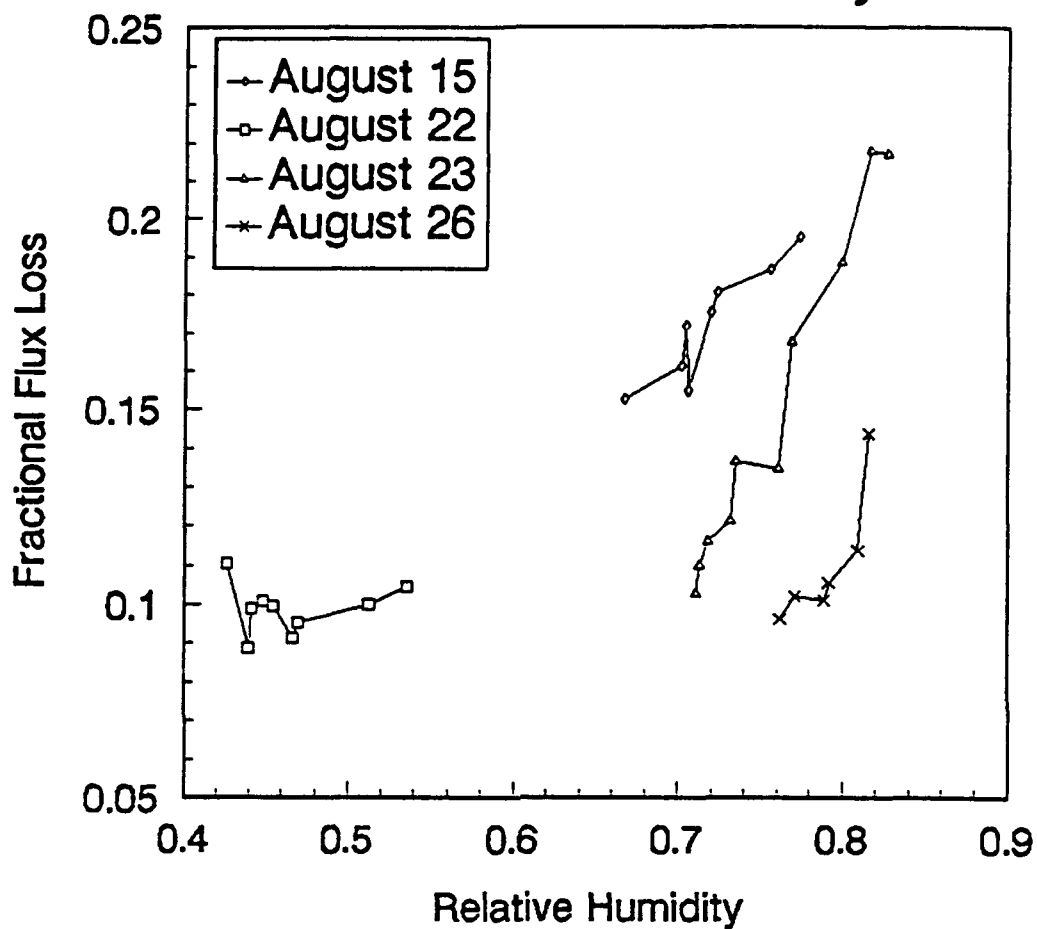


Figure 4.15. Fractional flux loss is shown as a function of relative humidity.

appears that fractional flux loss (which is probably more useful than net flux loss, since there is no cosine effect to consider) can be related to relative humidity, at least at values of the latter over 70%. Fractional flux loss is also seen to be a linear function of 519-nm optical depth, at least under the conditions in this experiment. More research along these lines will have to be conducted with reliable measurements of scattering coefficient or visibility before fractional flux loss can be parameterized. It appears that the equation will be of the form $\Delta F/F = f(\tau, RH, k_{ext})$, where RH designates relative humidity, with range limits set on the relative humidity. It is impossible from this research to provide a complete equation for $\Delta F/F$ because of unreliable visibility or scattering coefficient data.

Chapter 5

CONCLUSIONS AND RECOMMENDATIONS

Atmospheric aerosols are known to modify the earth's surface radiation budget by a combination of scattering and absorption of shortwave radiation. Since aerosol influences radiative transfer, it is assumed *a priori* that it affects climate as well. The Rock Springs experiment was designed to learn how anthropogenic sulfate aerosol affects the central Pennsylvania surface radiation budget and, by implication, the climate. With the investigation complete, the setup and goals of the experiment will be reviewed, and then discuss what was learned, what questions remain, and what could be done to improve conditions for future experiments along these lines.

The concept behind the Rock Springs experiment was relatively simple: take measurements of surface fluxes and standard meteorological variables at a site in rural central Pennsylvania, and attempt to infer the effects of the ambient aerosol loading on the surface radiation budget. The motivation was that while there have been many papers addressing the theoretical links between aerosol and climate (e.g., Schneider, 1989; Charlson et al., 1992), few studies have been done on regional climate effects arising from anthropogenic aerosol emissions. The research was conducted to obtain high-quality aerosol data and use them to reduce uncertainties in climate model parameterization.

Since this work targeted anthropogenic sulfate aerosols, the location of The Pennsylvania State University is an ideal choice at which to conduct experiments. The northeastern United States is certainly subject to large, anthropogenic perturbations in sulfate concentration (Ball and Robinson, 1982; Fraser et al., 1984). Furthermore, central Pennsylvania is centrally located within this large area, but has no large sulfur sources in its immediate vicinity. For these reasons, the ambient aerosol concentration well represents man's influence only and renders the experimental location nearly perfect.

With the site chosen and a concept in mind, all that remained was to focus the research, determine any necessary assumptions to be made, and begin taking measurements. To narrow the topic to a feasible scope, it was decided to examine only the direct effects of sulfate haze on the surface radiation budget (as opposed to investigating the indirect effects referred to in Chapter 1). Assuming the effect could be quantified, the secondary goal was to study the possibility of relating surface flux losses to relative humidity and/or visibility; these parameters were chosen because they are frequently measured and because they are theoretically tied to attenuation. Key assumptions were that the single-scattering albedo for sulfate particles is approximately unity (Hänel, 1980; Blanchet, 1989), carbonaceous material concentration was considered to be negligible, any sulfate present was presumed anthropogenic, and the scattering coefficient calculated at the surface was assumed constant throughout the boundary layer.

The basic questions asked at the end of every experiment should be, "What did we learn?", "What did we fail to learn?", and "What steps can we take to improve our next experiment?". These will be addressed one at a time with the hopes of explaining the net result of this research and of providing some guidance to future aerosol researchers.

Perhaps the most important data gleaned from the Rock Springs experiment were the magnitudes of the surface flux losses as calculated by the model. The primary goal of this research was to make a solid estimate of the degree to which sulfate haze attenuates radiation at the surface, and this goal was accomplished. The data expressed in terms of clear-sky insolation ranged from nine to twenty-five percent reduction. The lower end of this range is in good agreement with the results of Ball and Robinson (1982), who discovered annually-averaged irradiation depletion of 7.5% over the midwestern United States; the upper extreme of nearly 25% is slightly greater than the value of 20% obtained by Ball and Robinson (1982) on a hazy day.

In addition, it was found that the radiative transfer model used provided reliable estimates of aerosol effects. The algorithm, as shown in Chapter 3, verified well given user-defined optical depth data. All models fall short of perfectly duplicating the atmosphere, but the scheme employed here at least demonstrated the capacity to represent aerosol effects well. Its output can be treated as credible, and this or an improved version of the model can be used by other aerosol researchers.

The Rock Springs experiment also showed that an inexpensive, all-weather rotating shadowband radiometer (RSR) can likely be used in place of the more expensive and labor-intensive sun photometer. Though the RSR is less accurate than the sun photometer due to its wider field of view, this error was discovered to be a function of wavelength under the experimental conditions described and thus easily correctable. Future experimenters could save considerable money when measuring optical depths for extended periods.

Other interesting facts were learned during the course of this research. Attenuation due to sulfate haze was shown to be correlated to relative humidity when the latter was above 70%; the lack of connection at lower values agrees with the findings of Hänel and Zankl (1979). The relationship was particularly robust when fractional attenuation $\Delta F/F$ was considered; net flux loss ΔF is dependent on zenith angle and thus is not as strong a function of relative humidity as the fractional loss. Moreover, fractional flux loss was found to be related to the 519-nm optical depth linearly. The linear relationship between fractional flux loss and optical depth possibly is because the exponential term in transmission can be approximated as a straight line for small values of optical depth. It is not possible to extrapolate these results to other locations, and perhaps not even to different seasons in this area. However, if a linear relationship between fractional flux loss and optical depth can be confirmed by additional experiments, climate modelers would be aided in their attempts to represent sulfate aerosols mathematically.

This experiment was a success in that it answered the questions regarding size of fractional flux loss and relation to relative humidity and optical depth; it also allowed the possibility of monetary savings for future aerosol researchers by showing the feasibility of using a rotating shadowband radiometer.

Despite the many questions answered, there were setbacks. The visibility measurements lacked the precision needed to be of any use; it seems this was merely a matter of inadequate instrumentation and could be readily fixed with a more reliable nephelometer. Because of this failing, however, it is impossible based on this study to make any statements about the relationship of sulfate haze to visibility. Another problem encountered by the researchers was a shortage of information regarding the extent and evolution of the planetary boundary layer. The ceilometer used lacked the sensitivity necessary for this study. As with the visibility data, the root of this problem is instrumentation and could be solved by using a more accurate (but more expensive) lidar.

What can be learned from this experiment to aid future aerosol research? Many scientific facts were learned; estimates of aerosol attenuation and its connection to relative humidity and optical depth are important findings to be used. From an experimental point of view, further research in this direction should definitely include, in addition to the instruments used at Rock Springs, a lidar to measure reliably boundary-layer heights and a dependable nephelometer to assess scattering coefficient simultaneously with other variables. An aging chamber with controlled humidity might aid future researchers in connecting

relative humidity and flux reductions mathematically. Modeling experiments could also be done with various sulfate aerosol size distributions to determine which most closely approximates reality. From a theoretical standpoint, the effects of relative humidity on any given number of particle types must be examined to determine which classes of particles are more responsive to change and which are less so. The effects of aerosols on climate are currently poorly understood and can be grasped better only through the combined efforts of field researchers and climate modelers.

REFERENCES

- Ackerman, T.P., 1977: A model of the effect of aerosols on urban climates with particular applications to the Los Angeles Basin. *J. Atmos. Sci.*, **34**, 531-547.
- Albrecht, B.A., 1989: Aerosols, cloud microphysics, and fractional cloudiness. *Science*, **245**, 1227-1230.
- d'Almeida, G.A., P. Koepke, and E.P. Shettle, 1991: *Atmospheric Aerosols: Global Climatology and Radiative Characteristics*. A. Deepak, 561 pp.
- Ångström, A., 1929: On the atmospheric transmission of sun radiation and on dust in the air. *Geogr. Ann.*, **11**, 156-166.
- Ångström, A., 1961: Techniques of determining the turbidity of the atmosphere. *Tellus*, **13**, 214-223.
- Ball, R.J. and G.D. Robinson, 1982: The origin of haze in the central United States and its effect on solar radiation. *J. Appl. Meteor.*, **21**, 171-188.
- Blanchet, J.P., 1989: Toward estimation of climatic effects due to Arctic aerosols. *Atmos. Environ.*, **23**, 2609-2625.
- Charlson, R.J., S. Schwarz, J. Hale, R.D. Cess, J.A. Coakley, J.E. Hansen and D. Hofmann, 1992: Climate forcing by anthropogenic aerosols. *Science*, **255**, 423-430.
- Corell, R.W., 1990: The United States Global Change Research Program (US/GCRP): An overview and perspective on the FY 1991 program. *Bull. Amer. Meteor. Soc.*, **71**, 507-511.
- Davies, C.N., 1974: Size distribution of atmospheric particles. *J. Aeros. Sci.*, **5**, 293-300.
- Fitzgerald, J.W., W.A. Hoppel, and M.A. Vietti, 1982: The size and scattering coefficient of urban aerosol particles at Washington, D.C. as a function of relative humidity. *J. Atmos. Sci.*, **39**, 1838-1852.
- Fraser, R.S., Y.J. Kaufman and R.L. Mahoney, 1984: Satellite measurements of aerosol mass and transport. *Atmos. Environ.*, **18**, 2577-2584.
- Goody, R.M., 1964: *Atmospheric Radiation, Vol. 1, Theoretical Basis*. Clarendon Press, 436 pp.

- Hänel, G., D. Weidert and R. Busen, 1990: Absorption of solar radiation in an urban atmosphere. *Atmos. Environ.*, **24B**, 283-292.
- Hänel, G. and B. Zankl, 1979: Aerosol size and relative humidity: Water uptake by mixtures of salts. *Tellus*, **31**, 478-486.
- Hansen, J.E., W.C. Wong and A.A. Lacis, 1978: Mount Agung provides test of a global climate perturbation. *Science*, **199**, 1065-1068.
- Hansen, J.E., G. Russell, D. Rind, P. Stone, A. Lacis, S. Lebedeff, R. Ruedy, and L. Travis, 1983: Efficient three-dimensional global models for climate studies: Models I and II. *Mon. Wea. Rev.*, **111**, 609-662.
- Herman, B.M., S.R. Browning and J.A. Reagan, 1971: Determination of aerosol size distributions from lidar measurements. *J. Atmos. Sci.*, **28**, 763-771.
- Husar, R.B., N.V. Gilliani, J.D. Husar, C.C. Paley and P.N. Turen, 1976: Long range transport of pollutants observed through visibility contour maps, weather maps, and trajectory analysis. In *Preprints, Third Symp. Atm. Turbulence, Diffusion and Air Quality*, Raleigh, NC, Amer. Meteor. Soc., Boston.
- Junge, C.E., 1963: *Air Chemistry and Radioactivity*. Academic Press, 382pp.
- Junge, C.E. and R. Jaenicke, 1971: New results in background aerosols studies from the Atlantic Expedition of the R.V. Meteor, Spring 1969. *J. Aeros. Sci.*, **2**, 305-314.
- Kaufman, Y.J. and M.-D. Chou, 1993: Model simulations of the competing climatic effects of SO₂ and CO₂. *J. Climate*, **6**, 1241-1252.
- King, M.D., D.M. Byrne, B.M. Herman, and J.A. Reagan, 1978: Aerosol size distribution obtained by inversion of spectral optical depth measurement. *J. Atmos. Sci.*, **35**, 2153-2167.
- Lacis, A.A. and J.E. Hansen, 1974: A parameterization for the absorption of solar radiation in the Earth's atmosphere. *J. Atmos. Sci.*, **31**, 118-133.
- Lamb, D., 1994: Personal communication.
- Leaitch, W.R., J.W. Strapp, G.A. Isaac, and J.G. Hudson, 1986: Cloud droplet nucleation and cloud scavenging of aerosol sulphate in polluted atmospheres. *Tellus*, **38B**, 328-344.

- Meador, W.E. and W.R. Weaver, 1980: Two-stream approximations to radiative transfer in planetary atmospheres: A unified description of existing methods and a new improvement. *J. Atmos. Sci.*, 37, 630-643.
- Michalsky, J.J., J.L. Berndt, and G.J. Schuster, 1986: A microprocessor-based rotating shadowband radiometer. *Solar Energy*, 36, 465-470.
- O'Neill, N.T., A. Royer, P. Coté, and L.J.B. McArthur, 1993: Relations between optically derived aerosol parameters, humidity, and air-quality data in an urban atmosphere. *J. Appl. Meteor.*, 32, 1484-1498.
- Penner, J.E. and G.W. Mulholland, 1991: Global climatic effects of aerosols: The AAAR Symposium-An overview. *Atmos. Environ.*, 25A, 2433-2434.
- Pollack, J.B., O.B. Toon, C. Sagan, A. Summers, B. Baldwin and W. Van Camp, 1976: Volcanic explosions and climate change: a theoretical assessment. *J. Geophys. Res.*, 81, 1071-1083.
- Schneider, S.H., 1989: The greenhouse effect: Science and Policy. *Science*, 243, 771-781.
- Shettle, E.P. and J.A. Weinman, 1970: The transfer of solar irradiance through inhomogeneous turbid atmospheres evaluated by Eddington's approximation. *J. Atmos. Sci.*, 27, 1048-1055.
- Toon, O.B., C.P. McKay, T.P. Ackerman, and K. Santhanam, 1989: Rapid calculation of radiative heating rates and photodissociation rates in inhomogeneous multiple scattering atmospheres. *J. Geophys. Res.*, 94, 16,287-16,301.
- Twomey, S.A., 1959: The nuclei of natural cloud formation. II. The super-saturation in natural clouds and the variation of cloud droplet formation. *Geofis. pur. Appl.*, 43, 243-249.
- Twomey, S.A., 1977: *Atmospheric Aerosols*. Elsevier, 302 pp.
- Twomey, S.A., M. Piepgrass and T.L. Wolfe, 1984: An assessment of the impact of pollution on global cloud albedo. *Tellus*, 36B, 356-366.
- Wallace, J.M. and P.V. Hobbs, 1977: *Atmospheric Science: An Introductory Survey*. Academic Press, 465 pp.
- Yamamoto, G. and M. Tanaka, 1969: Determination of aerosol size distribution from spectral attenuation measurements. *Appl. Opt.*, 8, 447-453.